



# Global characterization of oscillating grid turbulence in homogeneous and two-layer fluids, and its implication for mixing at high Peclet number

Marie Poulain-Zarcos <sup>\*</sup>

*Institut de Mécanique des Fluides de Toulouse (IMFT), Université de Toulouse,  
CNRS, Allée du Professeur Camille Soula, 31400 Toulouse, France  
and Laboratoire des IMRCP, Université de Toulouse, CNRS UMR 5623,  
Université Paul Sabatier, 118 route de Narbonne 31062 Toulouse Cedex 9, France*

Matthieu J. Mercier <sup>†</sup>

*Institut de Mécanique des Fluides de Toulouse (IMFT), Université Toulouse, CNRS,  
Allée du Professeur Camille Soula, 31400 Toulouse, France*

Alexandra ter Halle 

*Laboratoire des IMRCP, Université de Toulouse, CNRS UMR 5623, Université Paul Sabatier,  
118 route de Narbonne 31062 Toulouse Cedex 9, France*



(Received 11 June 2021; accepted 27 April 2022; published 26 May 2022)

Oscillating grid turbulence (OGT) is a specific situation that enables us to investigate the equilibrium between the turbulent kinetic energy,  $k$ , and the dissipation rate,  $\epsilon$ , without any mean flow. One of its main features is that, in homogeneous fluids, the turbulence intensity decreases with the distance to the vibrating grid used to generate the forcing. OGT is thus usually described in terms of depth profiles of turbulent quantities. In this paper, we discuss experiments realized in two different setups, and we compare our results for all turbulent quantities with past studies. The results on the turbulent kinetic energy and the integral length scale lead us to propose a parametric model for the eddy viscosity,  $\nu_t$ , taking into account the spatial decay of the turbulence being slightly different from previous descriptions. Indeed, we find that  $\nu_t$  is best described as a constant value over a certain depth,  $H_s$ , before decreasing quickly as a power law in  $z^{-3/2}$ . The specific depth  $H_s$  is defined at the depth where a discontinuity of the integral length scale is observed. Physically, it corresponds to the depth at which the presence of the grid no longer influences the flow. We also describe OGT in the case of a two-layer fluid. The description of the turbulence at depths  $z$  far from the position of the interface  $h$  ( $0 < z/h < 0.6$ ) is very similar to the case of a homogeneous fluid, whereas the region near the interface ( $0.6 < z/h < 1$ ) is strongly altered by the presence of the fluid boundary. Surprisingly,  $\nu_t$  (unlike the other turbulent quantities) no longer depends on  $z$  in such a configuration. Finally, we investigate mixing processes at the interface in this context. Thanks to large field measurement (about the width of the tank), we were able to identify large-scale coherent structures as well as the turbulent flow. We discuss the entrainment law of the interface and its relationship with the Richardson number based on different definitions used in previous studies, as well as by using our observations of the turbulent flow properties at the interface. Our observations suggest that mixing at the interface in OGT is controlled by the turbulent flow properties at the interface but could also be influenced by weak mean flow features. This

<sup>\*</sup>Present address: Aix-Marseille Université, Marseille, France; marie.poulain.1@univ-amu.fr

<sup>†</sup>matthieu.mercier@imft.fr

could explain why it is difficult to discriminate a simple dependence of the training rate with the Richardson number.

DOI: [10.1103/PhysRevFluids.7.054606](https://doi.org/10.1103/PhysRevFluids.7.054606)

## I. INTRODUCTION

Oscillating grid turbulence (OGT) is a well-characterized type of turbulent flow, both for homogeneous and stratified fluids. For example, oscillating grid systems are used to simulate the turbulence induced by waves and wind, which are the main source of mixing in the upper layer of the ocean [1,2]. It is also used to study sediment or pollutant transport in homogeneous fluid based on the equilibrium between advection and diffusion processes [3–6].

The main results first shown by Thompson and Turner [7] and Hopfinger and Toly [8] are that the root mean square (rms) velocities in the  $x$  (horizontal) and  $z$  (vertical) directions, respectively  $U_{\text{rms}}$  and  $W_{\text{rms}}$ , decrease with the power law  $z^n$  in a homogeneous fluid [7,8]. For a grid with square bars, Thompson and Turner [7] found an exponent  $n = -1.5$  starting from the mean position of the grid, while Hopfinger and Toly [8] found an exponent  $n = -1$  starting from a virtual origin,  $z_v$ , defined as the position at which the integral lengthscale,  $L_{\text{int}}$ , becomes zero. This virtual origin is generally below the mean position of the grid at  $S/2 + 1 \pm 0.5$  cm, where  $S$  is the stroke [8]. de Silva and Fernando [9] mentioned that the exponent  $n$  is very sensitive to the origin of  $z$  taken, and they advised to use the virtual origin. However, several studies considered the mean position of the grid as the origin of  $z$  [4,10,11]. In the following, we will express all depth profiles from the distance of  $z_v$ . In our case, we denote  $z$  as the distance from  $z_v$ , and  $z'$  as the distance from the top position of the grid. In such a convention, the depth profiles of the rms velocities can be parametrized by

$$\langle U_{\text{rms}} \rangle_x = C_1 M^{1/2} S^{3/2} f_g z^{-1} \quad \text{and} \quad \langle W_{\text{rms}} \rangle_x = C_2 M^{1/2} S^{3/2} f_g z^{-1}, \quad (1)$$

where  $M$  is the grid mesh, and  $C_1$  and  $C_2$  are constants varying between 0.20 and 0.25 and 0.19 and 0.27, respectively [8,9,12]. These constants might depend on  $S$  and  $f_g$ , the grid frequency, however no clear relation is established for now, and most of the authors assume  $C_1$  and  $C_2$  as constant [8,13]. Based on Eq. (1) and assuming a local isotropy in the horizontal plane, the turbulent kinetic energy (TKE),  $k = \overline{u'^2} + 0.5\overline{w'^2}$ , can be parametrized by [14]

$$k = 0.5(2C_1 + C_2)^2 M S^3 f_g^2 z^{-2}. \quad (2)$$

Another modeling approach proposed by Matsunaga *et al.* [10] is based on analytical developments using a  $k$ - $\epsilon$  model for turbulence. Notably, the authors obtained a parametric law for  $k$ , which was considered to better describe the TKE over the entire water column,

$$k = k_0 \left[ \frac{\epsilon_0}{1.82k_0^{1.5} z + 1} \right]^{-5}, \quad (3)$$

with  $k_0$  and  $\epsilon_0$  the turbulent kinetic energy and the dissipation rate injected in the system by the grid, respectively. Depending on the value of the grid Reynolds number  $\text{Re}_g = f_g S^2 / \nu_f$ , where  $\nu_f$  is the kinematic viscosity of the fluid, one can write

$$k_0 = 0.0081 M^{-1/4} S^{9/4} f_g^2 \text{Re}_g^{1/2} \quad \text{and} \quad \epsilon_0 = 0.082 M^{-1} S^3 f_g^3 \text{Re}_g \quad \text{for} \quad \text{Re}_g < 5500, \quad (4)$$

$$k_0 = 0.6 M^{-1/4} S^{9/4} f_g^2 \quad \text{and} \quad \epsilon_0 = 0.45 M^{-1} S^3 f_g^3 \quad \text{for} \quad \text{Re}_g > 5500. \quad (5)$$

In the following, we define  $L_{\epsilon-k} = 1.82k_0^{1.5}/\epsilon_0$ , a characteristic lengthscale convenient to compare with observations. Recently, Rastello *et al.* [11] revised the model of Matsunaga *et al.* [10]. They supply a slightly different definition for  $k_0$  and  $\epsilon_0$  at low Reynolds number ( $< 1000$ ). These modeling approaches allow us to predict the vertical dependencies of other characteristic quantities such as the TKE flux, the dissipation rate  $\epsilon$ , or the turbulent eddy viscosity  $\nu_t$ .

Concerning the integral lengthscale, both the analytical predictions and direct observations suggest that

$$L_{\text{int}} = \beta z' + z_v, \quad (6)$$

with  $\beta$  an experimental constant being approximately 0.1 [7–9,15,16]. Although it was shown that  $\beta$  might depend on  $S$  and might be higher near the grid,  $\beta$  is generally considered constant [13,17].

OGT was also used to understand processes in stratified fluids, with the first study that of Rouse and Dodu [18]. In particular, some authors studied the evolution of the entrainment velocity,  $U_e$ , in two-layer fluids configurations [7,8,16,19–21]. Indeed, even if the deep ocean is linearly stratified, the presence of a sharp density can exist near the surface essentially due to thermal effects, impacting the vertical mixing of the upper ocean [22]. Typically, the interface can be seen as a wall for the vertical transport of turbulence. Consequently, there is a transfer from vertical to horizontal scales with a flattening of turbulent eddies near the interface; the flow is not isotropic anymore, and the transversal component,  $U_{\text{rms}}$ , is amplified [23]. Nevertheless, some mixing occurs with the position of the interface evolving slowly (compared to the grid frequency) with time. The entrainment rate,  $E$ , is defined as the ratio of the entrainment velocity,  $U_e = dh/dt$ , and a characteristic velocity of the turbulent flow at the interface,  $U_{\text{rms}}$ . Turner [24] was one of the first to propose an evolution of the entrainment rate as a function of the properties of the turbulent stratified flow prescribed by  $S$ ,  $f_g$ ,  $L_{\text{int}}$ , the density difference between the two fluid layers,  $\Delta\rho = \rho_2 - \rho_1$ , the position of the interface (or mixing layer),  $h$ , and the diffusivity of the stratifying agent,  $\kappa$ . This dependence has been investigated broadly since that work [3,8,15,16,21,24–26], suggesting that  $E$  should be a function of the overall Richardson number  $\text{Ri}$  defined as  $\Delta\rho g L_{\text{int}} / \rho_1 U_{\text{rms}}^2$ , and of the Peclet number  $\text{Pe} = (v_f / \kappa) \text{Re}$ , if the value for the latter is smaller than  $\sim 10^3$  [19,24,27]. In the specific case of a salinity density gradient studied in our work, the dependency with the  $\text{Pe}$  number can be neglected and the following relationship is proposed:

$$E \propto \text{Ri}^\gamma. \quad (7)$$

A value of  $-3/2$  for  $\gamma$  is found considering an appropriate Richardson number for each study [1], i.e., by choosing the adequate turbulent quantities in the definition of  $\text{Ri}$ . Nevertheless, it must be noted that these turbulent quantities are always estimated (or measured) in homogeneous fluid conditions. Thus the exponent of this power law is still an open question, especially for small  $\text{Ri}$ . Indeed, if  $\text{Ri} < 5$ , a smaller value of  $-1.2$  can be found for  $\gamma$  [15]. The entrainment law is based upon the theoretical assumption that mixing occurs by local interfacial instabilities and intermittent mixing processes induced by interfacial wave breaking initiated by turbulent eddies or instabilities, as described, for example, in Ref. [28] when the Richardson number is sufficiently large. The limit of  $E$  for very large values for  $\text{Ri}$  is also not adequately modeled by Eq. (7), which should be independent of  $\text{Ri}$  [24,26].

In this paper, we use particle image velocimetry measurements (PIV) to propose a revised parametric description of relevant turbulent quantities for OGT in a homogeneous and a two-layer stratified fluid, with the ultimate goal to parametrize the eddy viscosity, which has not been considered in previous work. We also investigate the mixing of the two-layer stratified case using experimental observations (PIV and density measurements). In Sec. II, we present the experimental setup and methods used in this study. Then, in Sec. III we discuss past models used to describe OGT in homogeneous fluid, and we proposed a simplified eddy viscosity model. In Sec. IV, we discuss to what extent OGT is modified in a two-layer fluid. Finally, in Sec. V we discuss the mixing induced at the interface, before concluding the paper.

## II. EXPERIMENTAL SETUP AND METHODOLOGY

### A. Experimental setup

The study has been performed in two experimental setups. The biggest one, with a glass tank of  $1 \times 1 \times 1 \text{ m}^3$ , is shown in Fig. 1. The smallest one has a tank with a height of 1.2 m and a cross

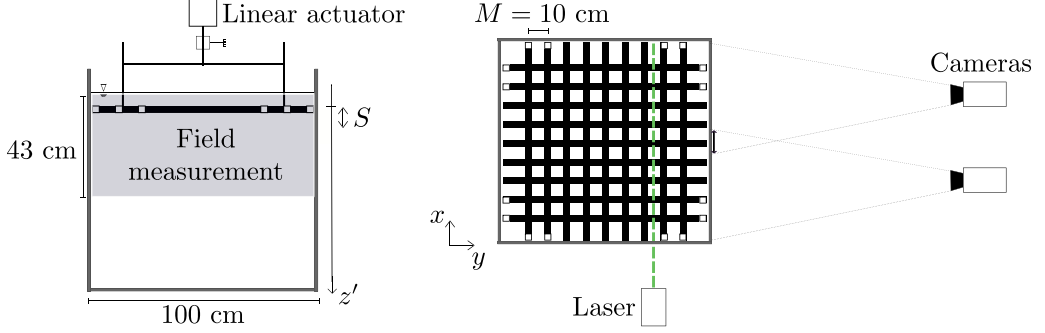


FIG. 1. Sketch of experimental setup 1.

section of  $0.4 \times 0.4 \text{ m}^2$ . In the following, setup 1 will refer to the biggest tank and setup 2 to the smallest one.

In both cases, the glass tank is filled with saltwater (NaCl) and the turbulence is generated by an oscillating grid. The highest position of the grid is kept 1.7 cm below the water surface. The water depth is 0.95 m in setup 1 and 1.00 m in setup 2. The grid is made of square bars of width  $M/5$ , with  $M$  the grid mesh ( $M = 10 \text{ cm}$  in setup 1 and  $M = 5 \text{ cm}$  in setup 2). The solidity of the grid is 34% (36%) in setup 1 (2). These values, below 40%, ensure the ability to minimize secondary flows [8,9,29]. As mentioned before, the grid oscillates vertically at the frequency  $f_g$  with a stroke  $S$ . Based on these two parameters, a Reynolds number is defined to characterize the stirring,  $\text{Re}_g = f_g S^2 / \nu_f$ , with  $\nu_f$  the kinematic viscosity of the fluid. Experimental parameters are reported in Table I.

In homogeneous fluid, the water density is  $\rho_f = 1042.0 \text{ kg/m}^3$ . In two-layer fluids, the upper layer is saline water with a density  $\rho_1$  and the bottom layer has a density  $\rho_2$  with  $\rho_2 > \rho_1$ . Before

TABLE I. Experimental parameters ( $S$  is the stroke,  $f_g$  is the oscillating frequency,  $\text{Re}_g$  is the Reynolds number based on the stirring, and  $\Delta\rho_{0i}$  is the initial density difference).

| #   | $S$ (cm) | $f_g$ (Hz) | $\text{Re}_g$ | Setup | Fluid       | $\Delta\rho_{01}$<br>( $\text{kg/m}^3$ ) | $\Delta\rho_{02}$<br>( $\text{kg/m}^3$ ) | Number of runs with $k/K > 10$<br>(total number of runs) |
|-----|----------|------------|---------------|-------|-------------|--|--|--|
| H1  | 8        | 2          | 12 550        | 2     | Homogeneous | 0  | 0  | 0 (4)  |
| H2  | 6        | 2          | 7190          | 2     | Homogeneous | 0  | 0  | 0 (4)  |
| H3  |          | 5          | 7980          | 2     | Homogeneous | 0  | 0  | 5 (6)  |
| H4  |          | 3          | 4790          | 2     | Homogeneous | 0  | 0  | 5 (6)  |
| H5  | 4        | 2          | 3190          | 2     | Homogeneous | 0  | 0  | 1 (6)  |
| H6  |          | 1.5        | 2400          | 1     | Homogeneous | 0  | 0  | 1 (1)  |
| H7  |          | 0.75       | 1200          | 2     | Homogeneous | 0  | 0  | 4 (4)  |
| H8  | 3.4      | 1.5        | 1730          | 1     | Homogeneous | 0  | 0  | 1 (1)  |
| H9  | 2        | 7          | 2790          | 2     | Homogeneous | 0  | 0  | 2 (4)  |
| H10 |          | 5          | 1200          | 2     | Homogeneous | 0  | 0  | 1 (6)  |
| H11 |          | 2          | 800           | 2     | Homogeneous | 0  | 0  | 1 (6)  |
| H12 |          | 2          | 800           | 1     | Homogeneous | 0  | 0  | 1 (1)  |
| H13 | 1.4      | 3          | 590           | 1     | Homogeneous | 0  | 0  | 0 (1)  |
| S1  | 4        | 1.5        | 2400          | 1     | Two-layer   | 2.8                                      |  | 2 (2)  |
| S2  | 3.4      | 1.5        | 1730          | 1     | Two-layer   | 2.2                                      | 1.1                                      | 2 (2)  |
| S3  | 2        | 2          | 800           | 1     | Two-layer   | 3.2                                      | 1.8                                      | 2 (2)  |
| S4  | 1.4      | 3          | 590           | 1     | Two-layer   | 3  | 1.2                                      | 2 (2)  |

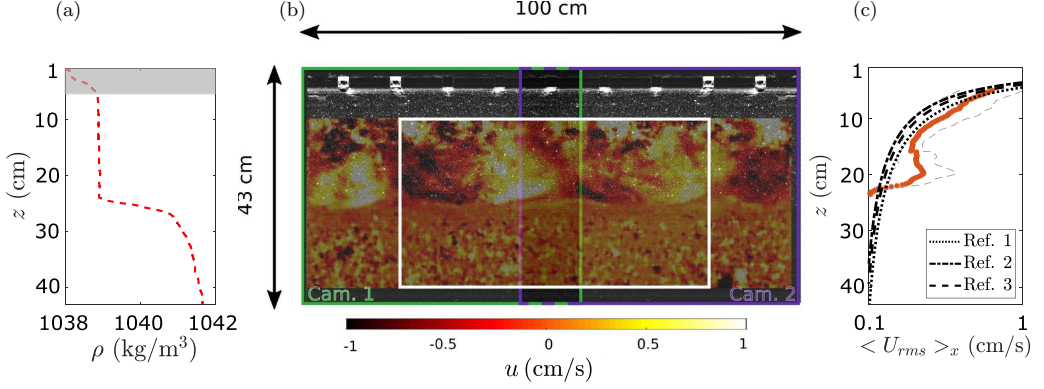


FIG. 2. (a) Density vertical profile from conductivity measurements. (b) Snapshot of the horizontal velocity field reconstructed after calculation. The green (violet) rectangles are the views from cameras 1 (2). The white rectangle indicates the area used to average turbulent quantities in the  $x$  direction. (c) Vertical profile of the horizontal rms velocity in the upper layer. Symbols are experimental data and dark lines are classical laws used in homogeneous flow. References 1–3 correspond to [12], [8], and [9]. Example of one of the two cases S3 at time  $t_3$ .

initiating the stirring, the interface is at  $h = 20$  cm below the water surface, and the density difference between the two fluid layers is  $\Delta\rho_{0i} = \rho_2(t=0) - \rho_1(t=0)$  kg/m<sup>3</sup>, with  $i = \{1, 2\}$  indicating different initial conditions as reported in Table I. To avoid distortion of the laser sheet and scatter of the light, an index-matching technique is carried out in the two-layer fluid configuration. It consists of adding ethanol in the proper proportions in the lightest fluid to have the desired density  $\rho_1$  with the same refractive index as the bottom layer. Here, since we have small density differences (but strong gradients), we add between 2% and 3% in mass ethanol to reach a refractive index of  $1.3434 \pm 0.0003$ .

### B. Conductivity measurements

In the two-layer fluid, due to the turbulent forcing of the interface, mixing occurs in the upper layer with an increase of  $\rho_1$  with time and a modification of the position and shape of the interface. To measure it, density profiles are recorded using a conductivity and temperature probe (MSCTI probe from PME©) in addition to PIV measurements described in Sec. II C. The conductivity probe is mounted on a motor-controlled translating shaft, hence it moves vertically from the water surface to 55 cm below it with a fixed speed of 5 mm/s to avoid disturbing the flow. The probe records samples at 500 Hz, which leads to a spatial resolution of 10  $\mu$ m; however, smoothing of the data in time (over 50 samples) is still done to reduce the level of noise, leading to an apparent resolution of 0.5 mm. The calibration in density is done before each experimental run, using six water samples with different densities encompassing the water density in the tank, while the calibration in temperature is valid for several days. For each experiment, seven density profiles are recorded: three in a “short” interval of time ( $t_1$  before the beginning of the stirring,  $t_2 = 17$  min,  $t_3 = 30$  min after initiation of the stirring) and four after a larger period of time ( $t_4 = 1$  h,  $t_5 = 2$  h,  $t_6 = 3$  h, and  $t_7 = 4$  h). An example of an obtained density profile is shown in Fig. 2(a). The position of the interface,  $h$ , as a function of time can be obtained from different definitions. One can use the position of the maximum value of the Brunt-Väisälä frequency,  $N^2 = -g\partial\rho/\partial z/\langle\rho\rangle_z$ , with  $g$  the gravitational acceleration and  $\langle\rho\rangle_z$  the vertical average of the water density. Alternatively, the definitions can be based on the depth of the mean density  $(\rho_1 + \rho_2)/2$  or on the mean depth of the density jump  $(z_1 + z_2)/2$ , with  $z_1$  such as  $\rho(z_1) = 1.15\rho_1$  and  $z_2$  such as  $\rho(z_2) = 0.85\rho_2$ . These values can differ since the density profile is not symmetrical; the largest difference in  $h$  between all these definitions is about 5% at the initial time step, and it decreases after 15 min of stirring until it is

less than 2% (not shown here). In the following, we define  $h$  as the altitude where the Brunt-Väisälä frequency is maximum.

### C. PIV measurements

The PIV field of view (almost 45 cm in height, over the full width of the tank in both setups), shown in Fig. 1 by the shaded area, is illuminated by a laser sheet (CFR 200 laser source, wavelength of 532 nm, 200 mJ max). In setup 1, it is fixed and located at  $x/L = 1/4$  from the border of the tank. In setup 2, the laser sheet is translated by a translating stage to allow measurements at  $x/L = 1/4$  and  $1/2$ . In both setups, the laser sheet thickness is approximately 1 mm.

To visualize the whole tank width with the same spatial resolution for the two setups, images are recorded using two sCMOS cameras mounted side-by-side, with a resolution of  $2160 \times 2560$  pixels in setup 1, and by only one camera in setup 2. They are located at 6.5 m (3.5 m) from the front face of the tank in setup 1 (2), leading to a field of view for each camera of  $43 \times 52 \text{ cm}^2$  ( $45 \times 40 \text{ cm}^2$ ) with an overlap of one mesh size (Fig. 1) between the two cameras. In setup 1, the spatial resolution for each camera being  $210 \text{ }\mu\text{m/pixel}$ , spherical particles of polystyrene ( $\rho_p \sim 1060 \text{ kg/m}^3$ ) with a diameter of  $228 \text{ }\mu\text{m}$  are used to characterize the flow. We verified that the particles are between 1.5 and 4 times smaller than the Kolmogorov scale. In setup 2, the spatial resolution is  $179 \text{ }\mu\text{m}$ , and we use spherical particles encapsulated by rhodamine with a diameter of  $50 \text{ }\mu\text{m}$  as tracers (their diameter being between 7 and 30 times smaller than the Kolmogorov scale). Thus they are tracers of the flow even if they are much larger than classical PIV particles [13,30,31]. To reduce their settling velocity, saltwater is used even in homogeneous fluid.

To resolve the oscillatory grid dynamics, especially just under the grid, the acquisition is done in sequential mode ( $Re_g < 3000$ ) or in double burst mode ( $Re_g > 3000$ ) depending on the stirring. Far away from the grid, the time step is increased artificially during the postprocessing in order to decrease the relative error on the displacement calculation, and thus on the velocity field. Typical values for the time step are chosen to achieve a mean displacement of 8 pixels at 30 cm below the water surface. The velocity fields are calculated using LAVISION software from Davis©. The final step of computations corresponds to interrogation windows of  $16 \times 16$  pixels with an overlap of 50%. The spatial resolution obtained is  $0.17 \times 0.17 \text{ cm}^2$  in setup 1 and  $0.14 \times 0.14 \text{ cm}^2$  in setup 2. The reconstruction of a snapshot of the horizontal velocity field,  $u$ , is shown Fig. 2(b), where the velocity fields from the two cameras in setup 1 are merged by averaging the velocity in the overlapping area of one mesh size, as mentioned before. It corresponds to grid parameters with  $Re_g = 800$  in the two-layer fluid configuration, 30 min after the beginning of the experiment (case S3). The interface is located 26 cm from the water surface, as shown in Fig. 2(a).

Fluctuating velocities in the  $x$  direction are defined such as  $u' = u - \bar{U} - u_g$ , with  $\bar{U}$  the temporal mean velocity and  $u_g$  the velocity associated with the grid frequency (respectively,  $w' = w - \bar{w} - w_g$  in the  $z$  direction). We choose to remove  $u_g$  to exclude the coherent mechanical stirring of the grid from the definition of the turbulent fluctuations. In our case, this flow represents between 5% and 10% of the turbulent kinetic energy (when defined as  $u' = u - \bar{u}$ ), until a depth of  $1.5M$  below the grid. This is in agreement with previous observations, which found a grid signature until  $z' \sim 2M$  below the grid [25]. Note that the harmonics of the grid forcing frequency are also present, but only really near the grid ( $z' < M$ ). Thus we do not consider them, their contribution being localized. We also verified that the side borders of the tank influence the flow until  $x \sim 1.5M$  from the wall, also in agreement with previous studies [32] (not shown). Therefore, we calculate depth profiles of turbulent quantities by averaging over the  $x$  direction excluding  $2M$  on each side [white rectangle in Fig. 2(b)]. In the following,  $\langle \rangle_x$  indicates the average in the  $x$ -direction. An example of the depth profile of the horizontal rms velocity,  $U_{\text{rms}} = (\overline{u'^2})^{1/2}$ , is shown in Fig. 2(c). For each stirring, 300 grid periods are recorded to ensure the statistical convergence of the data for both the mean field and the fluctuating one (not shown here).



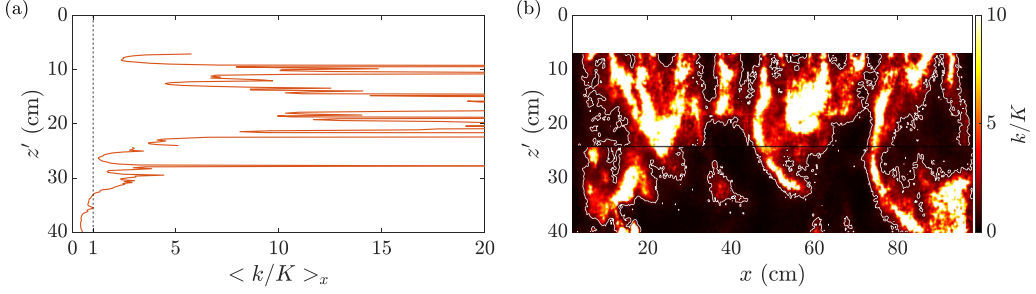


FIG. 3. Example for H12 of (a) depth profile of the turbulent kinetic energy,  $k$ , over the kinetic energy based on the mean flow,  $K$ , and (b) map of  $k/K$  to ensure that the turbulence is homogeneous. The white contour line represents  $k = K$ .

### III. CHARACTERIZATION OF OGT IN HOMOGENEOUS FLUID

In this section, we discuss OGT in a homogeneous fluid, and we describe in particular our approach to determine the eddy viscosity,  $\nu_t$ , taking into account the turbulence decay. Results are discussed in detail for the specific case H12 ( $\text{Re}_g = 800$ ), but the same trends are observed for all of the cases. The evolution of the parameters with the forcing is based on all observations. In Appendix A, the case H3 at high Reynolds number ( $\text{Re}_g = 7980$ ) is presented for the two illuminated planes. With regard to the discussion on the origin of the vertical coordinate in the Introduction, we stress here that we verified that taking  $z_v$  or the mean position of the grid does not have a significant impact on the exponents of the power law studied in this section.

#### A. Mean flow

In OGT, due to the finite size of the tank, mean flows can develop [29]. We verify that the flow is essentially controlled by the turbulence by comparing the TKE with the kinetic energy based on the mean flow,  $K$ . They are defined for our experimental data, respectively, as  $k = U_{\text{rms}}^2 + 0.5W_{\text{rms}}^2$  and  $K = \bar{u}^2 + 0.5\bar{w}^2$ . On the one hand, we verify that  $\langle k/K \rangle_x$  is larger than 1 [Fig. 3(a)]; on the other hand, we also verify that turbulence is homogeneous in the  $x$ -direction [Fig. 3(b)]. All of the cases presented in the following fulfill these conditions.

In some cases, especially in setup 2, the  $k/K > 10$  criterion can be obtained by limiting the depths for data analysis with a cutoff applied at the altitude for which  $k/K = 1$ . A summary of all the situations encountered is presented in the last column of Table I.

#### B. Turbulent properties

We first investigate the rms velocities, as shown in Fig. 4(a). The vertical profiles are in reasonably good agreement with the first model presented in Eq. (1), although a better agreement is obtained with the law proposed by de Silva and Fernando [9], with  $C_1 = 0.25$  and  $C_2 = 0.27$  for  $U_{\text{rms}}$  (not shown) and  $W_{\text{rms}}$ . Indeed, their law is closer to the analytical solution compared to the others, as was shown by Matsunaga *et al.* [10]. If one wants to compare the profiles to Eq. (3), where  $k$  is proportional to  $(z/L_{\epsilon-k} + 1)^{-5}$ , consequently we must consider  $U_{\text{rms}}$  and  $W_{\text{rms}}$  to be proportional to  $(z/L_{\epsilon-k} + 1)^{-5/2}$ . This power law, never tested before on the velocity profiles, is in really good agreement with our experimental data, both just under the grid and far from it where the turbulence decays. Note that the isotropy is discussed further (see Sec. IV B), but it is in good agreement with the literature [8] with  $U_{\text{rms}}/W_{\text{rms}} \approx 0.8$ .

For the turbulent kinetic energy, observations show a similar agreement with the literature in Fig. 4(b). At intermediate depths, where the turbulence intensity is large enough and not too close to the grid,  $k$  is in agreement with the power law  $z^{-2}$ . However, as observed for the rms velocities,

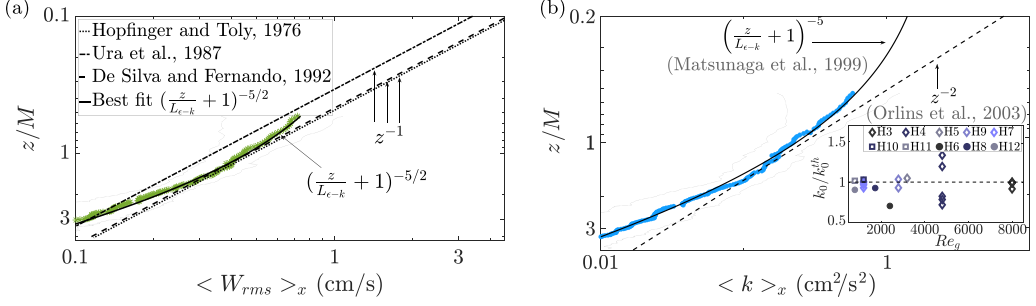


FIG. 4. Depth profiles of (a) the vertical rms velocity  $W_{rms}$  and (b) the turbulent kinetic energy,  $k$ . Symbols represent experimental data, with thin gray lines indicating the uncertainty in the values based on rms variations in  $W_{rms}$  and  $k$ . Black dashed lines represent the models in Eq. (1) or (2) with different values for the constants  $C_1$  and  $C_2$  associated with references; the solid black lines are best fit for a profile coherent with Eq. (3) based on experimental data. Inset plot in (b): comparison of the values for  $k_0$  obtained experimentally with its theoretical expression in Eq. (4) [10].

a power law of the type  $(z/L_{e-k} + 1)^{-5}$  better describes the profile for  $k$  over the entire water column. The fitting parameter  $k_0$  obtained experimentally is in reasonable agreement (about 6% on average) with the model in Eq. (4) [inserted plot Fig. 4(b)]. We are also in good agreement with Rastello *et al.* (about 10% on average, not shown here). Indeed, we are in a range where the two models have similar predictions. Note that the estimation of  $k_0$  from fitting the TKE or the rms velocities (in this case  $k_0 = U_0^2 + 0.5W_0^2$ ) leads to similar values, with a difference of about 10%.

We now discuss the evolution of the integral lengthscale  $L_{int}$ . We calculate it from the auto-correlation function of  $u'$  in the  $x$ -direction [33,34] to obtain its evolution with depth as shown in Fig. 5(a).  $L_{int}$  is close to the width of the grid bar, in agreement with previous works [6–9,30,35]. The empirical law in Eq. (6) is verified and allows us to estimate the proportionality constant  $\beta$ . We find two values for it, one near the grid and one in the region classically studied in OGT where the turbulence is considered homogeneous. Values of  $\beta$  are equal to 0.14 and 0.1, respectively, in agreement with previous studies mentioned before. No trend of  $\beta$  with  $Re_g$  is observed (not shown here). We define  $H_s$  as the altitude at which the discontinuity occurs [Fig. 5(a)]. This specific height is discussed with respect to the turbulence intensity in Sec. III C, but it has already been observed in previous work [13]. This discontinuity is certainly due to the presence of jets under each grid bar to

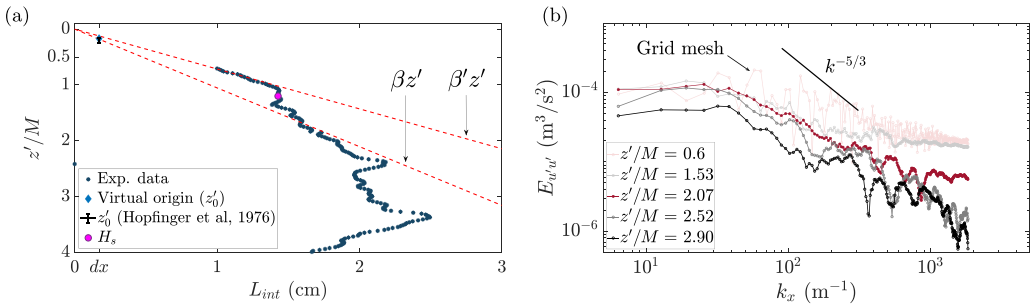


FIG. 5. (a) Depth profile of the integral lengthscale,  $L_{int}$ . The blue diamond is the virtual origin from the experimental data, found when  $L_{int} = dx$ , the spatial resolution. The error bar is the virtual origin from Hopfinger and Toly. Red dashed lines are Eq. (6) for two proportionality constants.  $H_s$  is the depth at which the discontinuity occurs. (b) One-dimensional energy spectra of  $u'$  for five vertical locations.



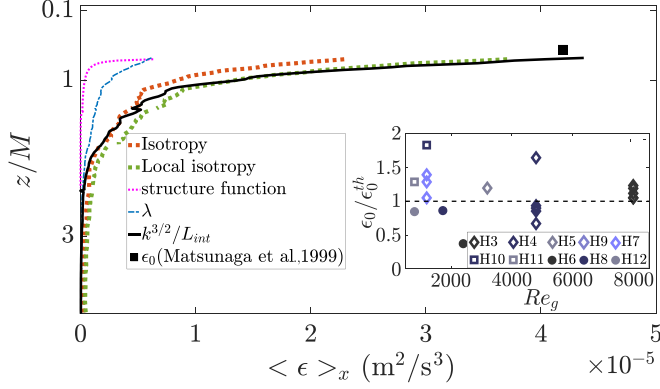


FIG. 6. Vertical profiles of the dissipation rate calculated from five definitions with different assumptions. Inset plot: comparison of  $\epsilon_0$  obtained experimentally with its theoretical expression in Eq. (4) [10].

almost one mesh below the grid (Appendix C). These coherent structures, observed in all cases in homogeneous fluid, have already been mentioned by McCorquodale and Munro [32].  $L_{\text{int}}$  obtained from the vertical fluctuating velocity has been calculated as well and shows the same tendency with  $z'$  (not shown here). We calculate it from the autocorrelation function of  $w'$  in the  $x$ -direction. Since the autocorrelation of  $w'$  in the  $x$ -direction is always smaller than the autocorrelation of  $u'$  in the  $x$ -direction, the integral lengthscale of  $w'$  is smaller than that of  $u'$ , especially near the grid, in agreement with the literature [13,35]. Finally, the virtual origin,  $z_v$ , is estimated by extrapolating  $L_{\text{int}}(z)$  up to the depth where it equals zero (at the limit of the spatial resolution for PIV). Note that we use the extrapolation far from the grid to compare our virtual origin with the literature (i.e.,  $L_{\text{int}} = \beta' z' + z_v$ ). We found  $z_v$  in agreement with the expression  $z_v = S/2 + 1 \pm 0.5$  cm proposed by Hopfinger and Toly [8] [error bar in Fig. 5(a)].

When comparing the results for  $L_{\text{int}}$  with the energy wave-number spectrum in Fig. 5(b), defined as the Fourier transform of the spatial correlation of the velocity fluctuations [34], this confirms that the quantification of the largest scales of the turbulence from a correlation analysis is a rigorous approach. Indeed, we indicate the lengthscale associated with the mesh size, which corresponds to a peak in the spectrum near the grid ( $z/M = 0.6$ ), thus the largest eddies of the turbulence are strongly influenced by the grid characteristics (mesh and bar size) [35]. One can observe that the inertial range characterized by the power law  $k_x^{-5/3}$  [33] is only observed over one decade due to two specific reasons: the low values of  $Re_g$  implying a low intensity of turbulence, and our spatial resolution ( $\approx 1.5$  mm), which is insufficient to resolve the Kolmogorov scale ( $< 1$  mm) [Fig. 5(b)].

We now investigate the dissipation rate,  $\epsilon$ , and first discuss the best way to estimate it over the entire water column. As presented in Fig. 6, we consider five alternative methods. For more details on each definition of dissipation rate, the reader may refer to Appendix B. A first method to calculate the dissipation rate is to use its definition from the velocity gradients in the three directions ( $x, y, z$ ). However, using PIV 2D-2C, only two velocity components are accessible. A classical way to overcome this is to assume global isotropy (*Isotropy* in Fig. 6) or at least local isotropy (*Local isotropy* in Fig. 6) [30,36–38]. Nevertheless, at depths between  $0M$  and  $2M$  below the grid, there is a strong signature of the grid geometry, thus the flow is not isotropic [8,13,14,32]. Furthermore, our spatial resolution is insufficient to solve the Kolmogorov scale [Fig. 5(b)]. Therefore, we consider the values of  $\epsilon$  based on these assumptions on velocity gradients to underestimate true values near the grid (red and green dotted lines in Fig. 6). The dissipation rate can also be obtained from the energy spectrum. However, this technique, which is based on the estimation of the slope of the energy spectrum in the inertial range, requires data covering at least two decades [10,38]. In our case, the inertial range is only observed over one decade due to low  $Re_g$ , i.e., low turbulence intensity [Fig. 5(b)], and we cannot consider the method. Another approach estimates  $\epsilon$  from the longitudinal

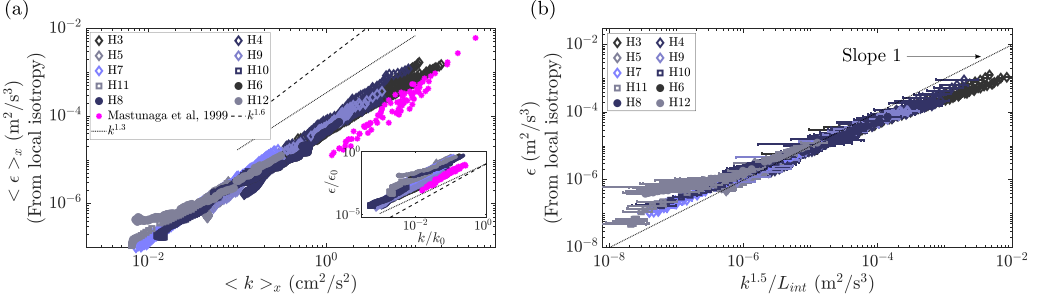


FIG. 7. (a) Dissipation rate  $\epsilon$  from the local isotropy assumption as a function of the turbulent kinetic energy,  $k$ , for all our runs. The data of Matsunaga *et al.* are also added [10]. The inset plot represents the same graph considering the normalized quantities. (b) Comparison between  $\epsilon$  from the local isotropy assumption and from  $k$  and the integral lengthscale.

structure function (*structure function* in Fig. 6) based on the first and second Kolmogorov similarity hypothesis [33,38]. However, even though this technique requires no assumptions on velocity gradients, it does assume “isotropy.” As stated before, especially under the grid, this leads to underestimated values of the dissipation (pink dotted line in Fig. 6). Finally,  $\epsilon$  can be calculated from characteristic lengthscales, namely the integral lengthscale [8,16,33] and the Taylor scale,  $\lambda$  [34], as shown by a black solid line and a blue dash-dotted line in Fig. 6, respectively. Note that the calculation based on the Taylor scale is also based on the assumption of global isotropy, which is why we exclude the definition of  $\epsilon$  based on the Taylor scale. A last method to obtain  $\epsilon$  from TKE and/or  $L_{\text{int}}$  is discussed in detail below. Matsunaga *et al.* mentioned that for OGT,  $\epsilon(z')$  and  $k(z')$  are related but that the definition  $\epsilon = k^{3/2}/L_{\text{int}}$  is not obvious if  $L_{\text{int}}$  is a linear function with  $z'$  and  $k \propto z'^{-2}$ . Actually, the authors defined  $L_{\text{int}} = k^{3/2}/\epsilon$  and found that  $L_{\text{int}} \propto z'$  while  $\epsilon \propto k^{1.7}$  from several experiments [10], which are reproduced in Fig. 7(a). We compare their observations with all our runs, with the values of  $\epsilon$  computed from the local isotropy assumption. Indeed, this definition is acceptable far away from the grid, and we extract data only from depths  $z'$  larger than  $1.5M$  to avoid underestimations. One can notice that a clear trend with  $k$  appears [Fig. 7(a)], which is best described by a power law  $\epsilon \propto k^{1.3}$  as indicated by a thin black line. Our results cover a larger range of values than those obtained by Matsunaga *et al.*, which we did find to increase slightly faster with  $k^{1.6}$  (not 1.7 actually), as indicated by a dashed black line. When comparing the values of TKE and energy dissipation rescaled by the predicted values at the grid ( $k_0$  and  $\epsilon_0$ ), as shown in the inset of Fig. 7(a), there is a greater scatter of the results, nevertheless the differences between the two datasets are less obvious, and both power laws could then be valid. It is worth noting that in the work of Matsunaga *et al.*, since  $k \propto z'^{-5}$  and  $\epsilon \propto z'^{-8.5}$ , then  $L_{\text{int}} \propto z'$ . In our case, we can thus consider that the values of  $L_{\text{int}}$  and  $k$  can predict  $\epsilon$ , since they are in agreement with the results in [10]; this is tested in Fig. 7(b). Some discrepancies are visible when turbulence is weak ( $\epsilon < 10^{-6} \text{ m}^2/\text{s}^3$ ), or for large values ( $\epsilon > 10^{-4} \text{ m}^2/\text{s}^3$ ), but that might be underestimated as discussed before.

To conclude, we consider  $\epsilon$  based on the definition with  $L_{\text{int}}$  as the best approach for our measurements. Its value at  $z' = S + d_b$  is in reasonable agreement with the value  $\epsilon_0$  provided by Matsunaga *et al.* [10] (black square in Fig. 6). A comparison of all the values of  $\epsilon_0$  obtained experimentally ( $\epsilon_0 = 1.82k_0^{1.5}/L_{\epsilon-k}$ ) with the model in Eq. (4) is shown in the inset in Fig. 6. A higher discrepancy than for  $k_0$  is observed with a difference of approximately 18% with the theoretical expression in Eq. (4), and about 22% with Rastello *et al.* [11] (not shown here). This is probably due to the addition of the uncertainties for both  $k_0$  and  $L_{\epsilon-k}$ . We checked that the origin of  $z$  (mean position of the grid or  $z_v$ ) does not affect either the discrepancy or the values of  $k_0$  and  $\epsilon_0$  (not shown here).

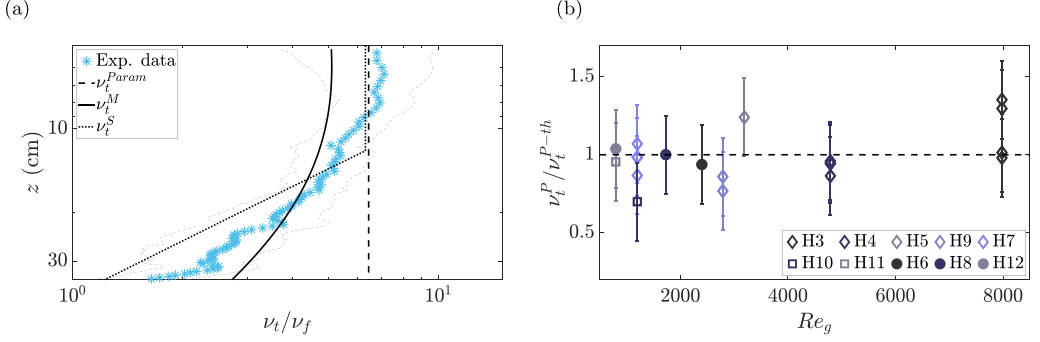


FIG. 8. (a) Depth profile of the eddy viscosity,  $\nu_t$ , normalized by the fluid kinematic viscosity  $\nu_f$ . Symbols are experimental data, with thin gray lines indicating the uncertainty in the values. Black lines are the parametric laws from Eqs. (9)–(11). (b) Comparison of  $\nu_t^P$  as a mean value of experimental  $\nu_t$  over  $H_s$  and the theoretical expression Eq. (8),  $\nu_t^{P-th}$ .

### C. Turbulent eddy diffusivity

We conclude this characterization of the turbulence by computing the eddy viscosity  $\nu_t$ , using the  $k$ - $\epsilon$  model with the definition of  $\epsilon = k^{3/2}/L_{int}$ . In this context, we can write

$$\nu_t = 0.09k^2/\epsilon = 0.09\sqrt{k}L_{int}. \quad (8)$$

The corresponding vertical profile of  $\nu_t$  is presented in Fig. 8(a) and compared to three models defined below. The first two models are obtained by substituting Eq. (2) and (6) into Eq. (8) for  $\nu_t^P$ , and by substituting Eqs. (3) and (6) into Eq. (8) for  $\nu_t^M$ , leading to

$$\nu_t^P = 0.09\beta(C_1^2 + 0.5C_2^2)\sqrt{M}S^{3/2}f_g, \quad (9)$$

$$\nu_t^M = 0.09k_0^{1/2}\beta z\left(\frac{z}{L_{\epsilon-k}} + 1\right)^{-5/2}. \quad (10)$$

Both models give the opportunity to predict the eddy viscosity profile if we use the value for  $\beta$  measured near the grid [Fig. 5(a)]. We verified that for all stirrings,  $\nu_t^P$  is a good approximation for the eddy viscosity near the grid, over a certain depth  $H_s$  [Fig. 8(b)]. However, it does not catch the turbulence decay, unlike  $\nu_t^M$ , which qualitatively catches it. Nevertheless,  $\nu_t^M$  underestimates the eddy viscosity near the grid and overestimates it far from the grid. This is partly explained by the variability in  $\beta$ .

As a better fit for the experimental observations, we propose a simplified model  $\nu_t^S$ , which combines features from both  $\nu_t^P$  and  $\nu_t^M$ ,

$$\nu_t^S = \begin{cases} \nu_t^P & \text{if } z < H_s, \\ \alpha z^{-3/2} & \text{if } z > H_s, \end{cases} \quad (11)$$

where  $\alpha$  and  $H_s$  are adjusted for each experiment. Here we have simplified the power law in  $z$  for depth larger than  $H_s$  since for all cases we verified that  $H_s/L_{\epsilon-k}$  is always much greater than 1 (between 50 and 200 typically). This pragmatic model is shown in Fig. 8(a) by the dotted curve. It seems to better describe the behavior of  $\nu_t$  and especially its decay. One of the major knowledge gaps in the description of  $\nu_t^S$  is the value for  $H_s$ . We remind the reader that  $H_s$  corresponds to the height at which the discontinuity of  $L_{int}$  occurs [Fig. 5(a)]. It seems to be a good cutoff scale for the eddy viscosity. Indeed, estimating  $H_s$  directly from  $\nu_t(z)$  (not shown here) leads to similar values of  $H_s$  estimated from the integral length scale. Even if a more complete dataset is needed, no grid

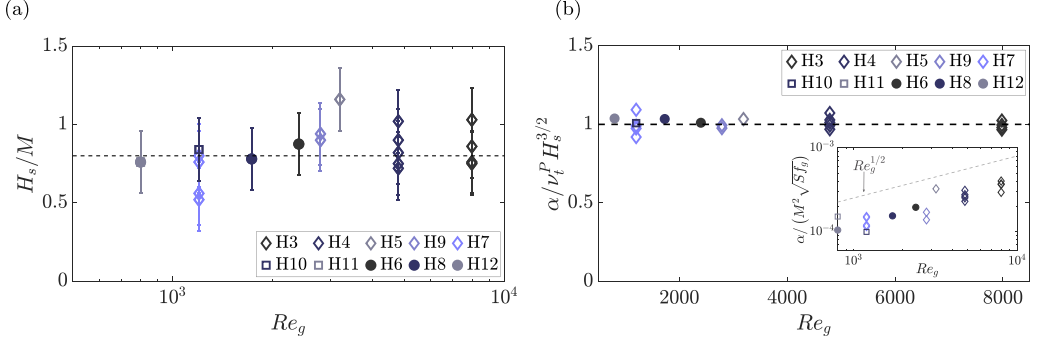


FIG. 9. (a) Evolution of  $H_s$ , the depth over which the eddy viscosity is almost constant, as a function of the grid Reynolds number,  $Re_g$ . Here  $H_s$  is expressed as the distance under the grid. (b) Evolution of  $\alpha$ , the proportionality constant of  $\nu_t^s$  when  $z > H_s$ , as a function of the Reynolds number.

Reynolds number dependence appears for  $H_s$  with

$$H_s \simeq 0.8 M \quad (12)$$

under the grid [Fig. 9(a)]. By evaluating Eq. (11) at  $z = H_s$ , we can deduce the expression for  $\alpha$ ,

$$\alpha = \nu_t^P H_s^{3/2}. \quad (13)$$

This is well verified experimentally [Fig. 9(b)]. Note that a dependence with  $M$ ,  $S$ ,  $f_g$ , and  $Re_g$  is observed [inset in Fig. 9(b)]. Once again, there is a good agreement with the dependence as expected. Indeed, from Eqs. (9) and (12) we deduce that  $\nu_t^P \propto (MSf_g Re_g)^{1/2}$  and  $H_s \propto M$ . Consequently from Eq. (13),  $\alpha$  should be proportional to  $M^2(Sf_g Re_g)^{1/2}$ , which we found experimentally [inset in Fig. 9(b)]. To our knowledge, there are no data in the literature measuring the eddy viscosity in grid turbulence to compare with this approach, which we summarize as Eqs. (11)–(13).

#### IV. CHARACTERIZATION OF OGT IN TWO-LAYER FLUIDS

We now investigate OGT in the case of a two-layer fluid, and in particular we compare it with its counterpart in homogeneous fluid. The major difference is the presence of the interface, which acts as a barrier at a certain depth for the turbulence. The depth of the interface slowly moves away from the grid with time as mixing occurs. For each case, the position of the interface is initially farther than the distance  $H_s$  from the grid, as shown in Fig. 10. Note that the distance  $H_s$  is deduced from Eq. (12). For the comparison of profiles at various times, we will use the vertical coordinate as well as a nondimensional coordinate using the position of the interface  $h$  for the two-layer fluid, and  $H_s$  for the homogeneous one to rescale the  $z$ -axis. For each value of  $Re_g$ , the instants at which the turbulent properties are computed are labeled  $t_i$ , with  $2 \leq i \leq 8$ . Each PIV measurement is associated with two density profiles recorded by the conductivity and temperature probe. Only the two first instants are associated with one density profile because of experimental constraints (Fig. 10).

##### A. Mean and coherent flows

In the two-layer case, we ensure again that the turbulent intensity is higher than the mean flow in the upper layer (not shown). We remind the reader that the interface acts as a barrier (no motion below the interface is observed), thus in the following we only discuss the flow for  $0 < z < h$ . For all cases, the mean flow is stronger than in the homogeneous case, as illustrated for the case of S3 in Fig. 11. Near the interface, regular patterns are observed [Figs. 11(b) and 11(e)]. These patterns persist over time [Figs. 11(c) and 11(f)] and they are systematically present for all stirrings. Between experiments, the only difference is the number of patterns, which varies between two and

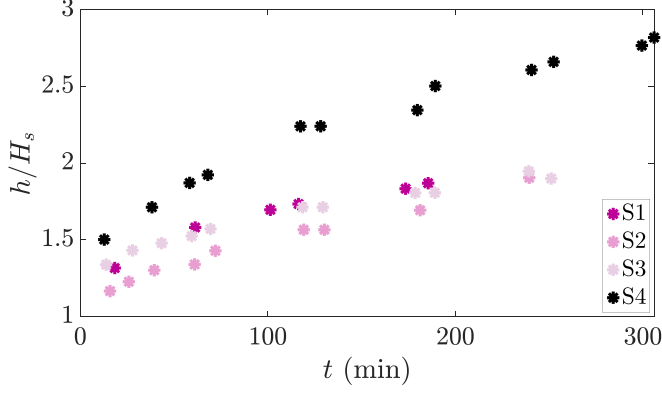


FIG. 10. Time evolution of the position of the interface,  $h$ , normalized by the depth  $H_s$  over which the eddy viscosity is almost constant.

four depending on  $f_g$ , but we do not explain this dependence. We can see that these patterns are the signature of the transfer from vertical scales to horizontal ones. Indeed, looking at the vertical mean velocity component, the mean flow seems to be organized in jetlike structures, as observed in Figs. 11(e) and 11(f). We also note that these structures are different from those in homogeneous fluid [Fig. 11(d)]. Indeed, for this case, finer jets are observed under each grid bar, and vertical flow is dominant near the grid ( $z/M < 1.5$  and  $20 < x < 80$  cm) and near the side walls ( $x < 20$  cm and  $x > 80$  cm).

We also investigated the presence of internal waves in the velocity data, especially near the interface, and more details are presented in Appendix D. A weak signature of internal wave dynamics is visible in the density spectrum of both the horizontal and vertical velocity components, for depths between  $0.8h$  and  $h$ . Overall, the energy of the signal for internal waves is small compared to the one related to turbulence above the interface ( $z/h \leq 0.6$ ).

### B. Overall turbulent properties (far from the position of the interface)

First, we discuss the turbulent properties far from the position of the interface. We focus on what happens in the vicinity of the interface in Sec. IV C.

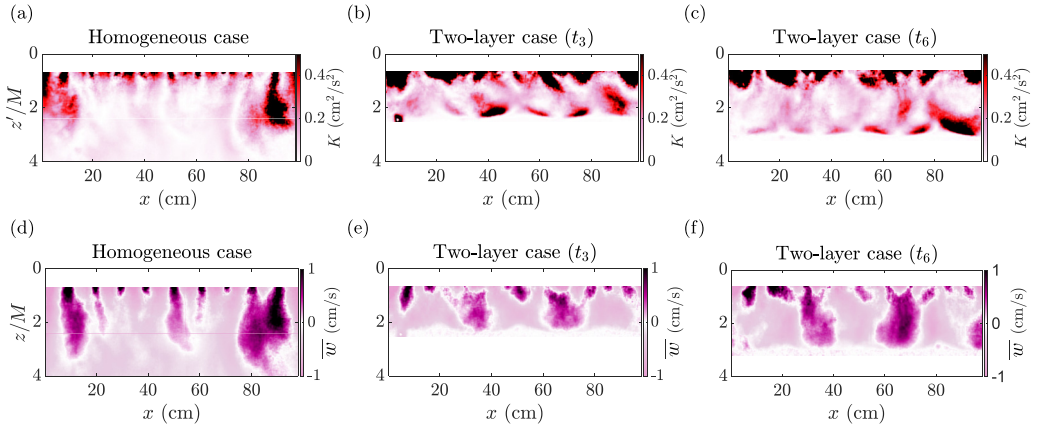


FIG. 11. Examples of maps of the mean kinetic energy  $K$  (top) and vertical velocity  $\bar{w}$  (bottom), in (a),(d) homogeneous fluid (case H12), and (b),(c),(e),(f) two-layer fluid at two different times (case S3).

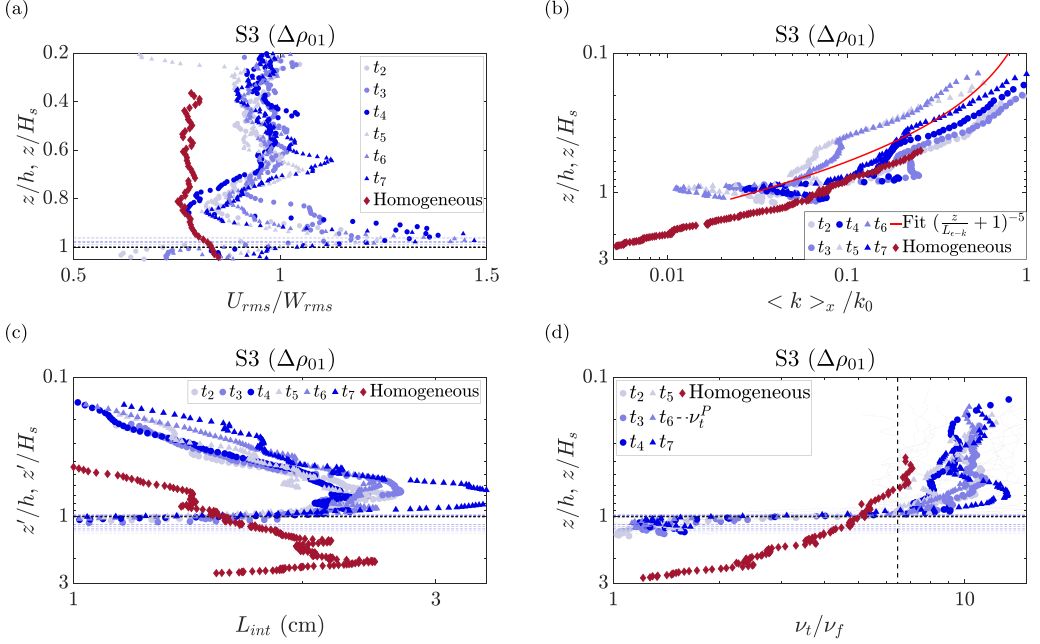


FIG. 12. Depth profiles of (a) the isotropy degree, (b) TKE, (c) integral lengthscale, and (d) turbulent eddy diffusivity, with the  $z$ -axis starting from the top position of the grid normalized by  $h$  for the two-layer fluid and by  $H_s$  for the homogeneous fluid; for case S3 ( $\Delta\rho_1$ ).

We start the discussion with the loss of isotropy near the position of the interface [Fig. 12(a)]. Indeed,  $U_{rms}/W_{rms}$  is no longer constant in the vicinity of  $h$ , unlike the case in homogeneous fluid. This phenomenon, well known in the literature, corresponds to the energy transfer from vertical to horizontal scales [8,20,23]. From our experimental data, it seems that the loss of isotropy appears after a depth of  $0.6h$  to  $0.8h$ . Thus, the interface can affect the flow over a significant depth above it. One can also notice in Fig. 12(a) that the maximum value for  $U_{rms}/W_{rms}$  is always reached at a depth,  $z_{Max Iso}$ , smaller than  $h$  (indicated by horizontal dashed lines). In the following section, we discuss in greater detail where this maximum value occurs, which may be related to the mixing processes that take place in the upper layer only [18,23].

We now look at the turbulent kinetic energy profiles in Fig. 12(b). If we focus more on the upper part of the fluid (near the grid), there is not a big difference between homogeneous and two-layer cases for depths smaller than  $0.6h$  (also true without the normalization of the  $z$ -axis). The parameter estimates from the homogeneous models, such as Eq. (4), can be estimated by fitting the profiles over  $[0, 0.6h]$ , and their evolution with time is shown in Fig. 13(a). Other than at large times, when the TKE no longer decreases like in the homogeneous case and thus  $k_0$  (through  $L_{\epsilon-k}$ ) is affected [Fig. 12(b)], the values for the parameters are quite constant, with  $k_0/k_0^H$  of the order of  $0.80 \pm 0.22$ .

Similarly, we can study the integral lengthscale profiles in Fig. 12(c), and we discuss their shape with time and with two specific regions of interest. To begin with, note that  $L_{int}$  is still of the order of the grid bars. At a fixed depth, the integral lengthscale is generally larger in the two-layer fluid than in the homogeneous case (the difference between the two near the grid is small if one compares nonstretched profiles). Secondly,  $L_{int}$  no longer appears as a piecewise function with a clear discontinuity as in the homogeneous case. This could be explained by a different flow under the grid in the case of a two-layer fluid, as detailed in Appendix C. Indeed, in the stratified case the jets under the grid bars disappear, and larger structures appear up to  $1.5M$  under the grid. Finally, a clear difference appears with a strong peak for  $L_{int}$  before it tends to zero when it reaches the



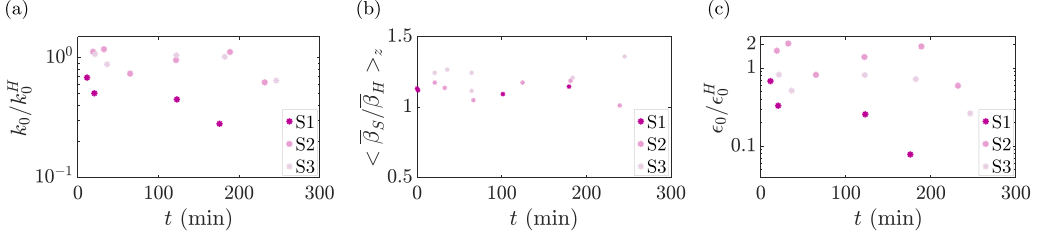


FIG. 13. Temporal evolution of (a)  $k_0$  normalized by the  $k_0^H$  measured experimentally in homogeneous fluid, and (b) the proportionality constant  $\beta_s$ , for the integral lengthscale from Eq. (6), normalized by the proportionality constant in homogeneous fluid  $\beta_H$ , (c)  $\epsilon_0$  normalized by the  $\epsilon_0^H$  measured experimentally in homogeneous fluid.

interface. We will see in the next section that the peak value of  $L_{\text{int}}$  plays a key role in the description of the turbulent quantities in two-layer fluid.

Finally, from the two quantities studied, namely  $k$  and  $L_{\text{int}}$ , one can combine them to compute the dissipation rate and the eddy viscosity, shown in Fig. 12(d). The evolution of  $\epsilon_0/\epsilon_0^H$  is shown in Fig. 13(c). As in homogeneous fluid, due to the addition of uncertainties of  $k_0$  and  $L_{\epsilon-k}$ , a higher discrepancy than for  $k_0$  is observed. From our data,  $\epsilon_0/\epsilon_0^H$  is quite constant and of the order of  $0.9 \pm 0.6$ , and it is difficult to conclude about a quantitative difference between OGT in two-layer fluids and in homogeneous fluids in the upper part of the fluid, far enough from the interface. However, we observe a clear difference in the profiles near the interface. Nevertheless, in the two-layer fluid  $\nu_t$  turns out to be almost constant with  $z$  before it sharply decreases to  $\nu_f$  in the vicinity of the interface. This is quite surprising since in the homogeneous fluid  $\nu_t$  is almost constant over a certain depth,  $H_s$ , before decreasing with power law  $z^{-3/2}$ . As already mentioned, our experiments are with  $h > H_s$  (Fig. 10) at all times, hence the decay should have been observed if it existed. We can thus conclude that in the two-layer case, the turbulence decay over depth is canceled or at least put off by the presence of the interface until  $h > 2H_s$ , although this bound shall be investigated in a specific study. It could be explained by the simultaneous increase of TKE and  $L_{\text{int}}$  near the position of the interface due to the confinement of the energy in the upper layer. It is also interesting to note that the temporal variability observed regarding the eddy viscosity is weak [Fig. 12(d)], suggesting that describing OGT using  $\nu_t$  instead of TKE, as it is usually done, can be a simpler approach. For the highest stirrings ( $\text{Re}_g = 2400$  and  $1730$ ), the parametric law  $\nu_t^P$  from homogeneous fluid is a good approximation for  $\nu_t$  (see Fig. 25 in Appendix E). However, for the lowest stirrings ( $\text{Re}_g = 800$  and  $590$ ), it leads to underestimations of about 35% of the eddy viscosity [Fig. 12(d)]. It could be of interest to investigate in more detail the reasons for this discrepancy in  $\nu_t^P$ . More experiments on a larger range of Reynolds number have to be performed to confirm it.

### C. Turbulent properties near the interface

We now look at turbulent quantities in the vicinity of the interface ( $0.6 < z/h < 1$ ). We discuss how the loss of isotropy and the increase of both TKE and  $L_{\text{int}}$  occur linked to the flow scales. In the following, we will preferentially use the peak value of the integral lengthscale, which we denote as  $L_{\text{int}}^{\text{max}}$ , as a reference lengthscale. Comparing  $L_{\text{int}}^{\text{max}}$  with the integral lengthscale at the position of the interface in homogeneous fluid,  $L_{\text{int}}^H$ , we find from our experimental data that  $L_{\text{int}}^{\text{max}} = 0.9L_{\text{int}}^H$  (not shown). This is in agreement with results obtained near a solid boundary [39]. Moreover, as illustrated in Fig. 14(a) for case S3, the decrease of  $L_{\text{int}}$  occurs at  $(z' - h) \simeq L_{\text{int}}^{\text{max}}$  to reach  $0.6L_{\text{int}}^{\text{max}}$  at  $(z' - h) = 0$ , like in OGT near a solid boundary [39]. We also compared the peak of the integral lengthscale with the interface thickness,  $\delta h$ , but no clear correlation was observed (see Sec. V).

If we look at the distance from  $h$  where the loss of isotropy occurs [Fig. 12(a)], it seems that the location of the peak of anisotropy evolves slowly with time. At early times ( $t < 60$  min), it occurs at  $0.7(\pm 0.3)L_{\text{int}}^{\text{max}}$  above  $h$ , while at large times ( $t > 60$  min), except for  $\text{Re}_g = 1730$ , it

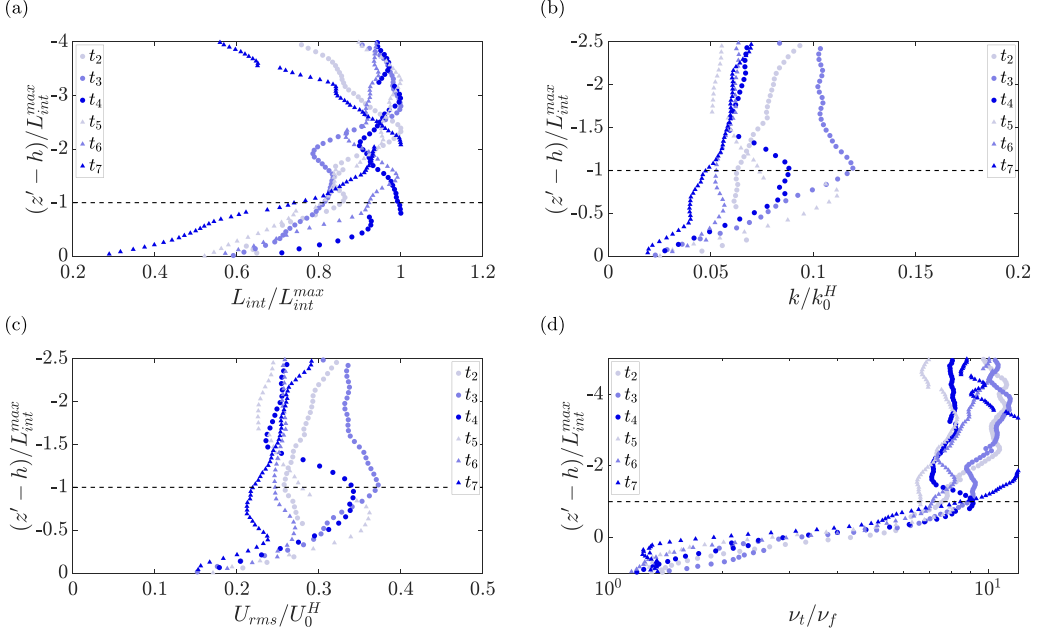


FIG. 14. Depth profiles of (a)  $L_{int}$ , (b) TKE, (c) rms horizontal velocity normalized by the same quantity at  $z = h$  in the homogeneous fluid case, and (d) the eddy viscosity normalized by the kinematic viscosity of the fluid. The vertical axis now starts from the position of the interface,  $h$ , and is normalized by  $L_{int}^{max}$ . Zoom on case S3 ( $\Delta\rho_1$ ) in the region  $0.6 < z/h < 1$ .

occurs at  $0.4 (\pm 0.2) L_{int}^{max}$  above  $h$ . We do not clearly understand this decrease. Despite this, on average over all times we found that the peak of anisotropy occurs at  $0.55 (\pm 0.25) L_{int}^{max}$  above  $h$ . This is again in reasonable agreement with results near a solid boundary [39], where the peak occurs between  $0.7 L_{int}^{max}$  and  $L_{int}^{max}$  above the plate. Our data are also in good agreement with a study of OGT in two-layer fluid [23], which uses the integral lengthscale at  $z = h$  in homogeneous fluid instead, and which found  $z_{Max Iso}$  close to  $0.6 L_{int}^H$  above  $h$  [23]. Regardless of the definition of the integral lengthscale, we observe that the transfer from vertical to horizontal scale occurs always from the position of the interface (in the upper layer). More precisely, it occurs at about  $0.6$  integral lengthscale above the position of the interface. This confirms that the mixing processes take place in the upper layer only [18,23].

Similarly, we can study the TKE in the region  $0.6 < z/h < 1$ , where a peak is observed. There is a strong temporal variability, with a loss that can reach 20% of the initial TKE in 3 h for some cases (S2, not shown). To highlight this aspect, the  $z$ -axis is rescaled with respect to the integral lengthscale as well [Fig. 14(b)]. At early times ( $t_2$  and  $t_3$ ), when the steady state is not necessarily reached, there is an increase of the TKE at  $(z - h) = L_{int}$ . At later times ( $t_i > t_3$ ), the peak appears at  $(z - h) \approx 0.5 L_{int}$ . This is in reasonable agreement with results in two-layer fluid [23] and near a solid boundary [39], where a maximum of TKE was found at  $(z - h) \approx 0.3 L_{int}$ . The peak of TKE is linked with the transfer from the vertical to the horizontal scales. More precisely, it is due to the local increase of  $U_{rms}$ , as shown in Fig. 14(c), with the peak value of the horizontal fluctuating velocity having a similar evolution to that of the TKE. The variation of the peak intensity is consistent with the fact that the energy that would diffuse in the rest of the tank is now trapped in a layer of increasing depth. A classic way to discuss this aspect is to use the vertical flux of TKE,  $\overline{k'w'}$  [23,39]. However, from our experiments this quantity is too noisy to draw any conclusions (not shown).

Finally, we focus on the eddy viscosity in the vicinity of the interface. We observed that  $\nu_t$  decreases below  $z = L_{int}^{max}$  [Fig. 14(d)], with all the curves collapsing in a single trend. At the

interface ( $z' = h$ ), the eddy viscosity is really weak ( $\nu_t < 3\nu_f$ ). Once again, this confirms that the turbulence is trapped in the upper mixed layer.

#### D. Synthesis

In conclusion, in the region  $0 < z/h < 0.6$ , no significant difference of the turbulent quantities between the OGT in homogeneous or two-layer fluid is observed. On the contrary, near the position of the interface, in the region  $0.6 < z/h < 1$ , there is a loss of isotropy and a clear increase of values for TKE and  $L_{\text{int}}$  compared to the homogeneous case, which results in a nearly constant value of  $\nu_t$  with depth. These differences are due to (i) the transfer from the vertical scales to the horizontal ones, and (ii) the confinement of the TKE in the upper layer, both induced by the presence of this deformable interface. Similar observations have been obtained previously in OGT studies with a two-layer fluid or near a solid boundary [23,39], where it was identified that the isotropy and the maximum increase of the turbulent quantities occur about one integral lengthscale above the boundary (interface or rigid plate).

Overall, in terms of the description of the eddy viscosity, we observed that  $\nu_t$  is nearly constant over the range  $0 < z/h < h - L_{\text{int}}^{\text{max}}$ , and sharply decreases to  $\nu_f$  over the distance of one integral lengthscale. The parametric model  $\nu_t^P$  in Eq. (9) can be used for the estimate over the entire depth  $h$  (although  $h/H_s > 1$ ), with a tendency to underestimate (about 35%) the observed values at  $\text{Re}_g$  smaller than 1700.

### V. MIXING

The mixing is related to the spatial evolution of the interface. It is well known that in the setup considered here, the thickness of the interface and the density difference evolve with time [3,18]. To fix the position of the interface, some authors used two oscillating grids on each side of the interface [19]. Others tried to maintain a constant density difference,  $\Delta\rho$ , between the two fluid layers, adding fresh water in the stirred layer [17]. However, in each case the steady state was not reached. Indeed, to ensure a steady state, both the position of the interface and the density difference have to remain constant, as mentioned by Verso *et al.* [16], who proposed an interesting model based on the flux balance to characterize the entrainment and thus the mixing. To apply this model, a specific setup is needed with inflows and outflows of water. Our setup cannot be transformed with inlets/outlets, consequently both the interface and the density difference evolve with time.

In this section, we investigate the time evolution of the interface depending on the stirring. Then we discuss the nature of the turbulence decay in terms of the entrainment rate. Finally, thanks to our large field measurement, we discuss the erosion process in our case of OGT.

#### A. Position of the interface with time

Previous studies have mainly investigated the mixing in terms of temporal evolution of the interface. Before discussing it in more detail, we mention that the variation of  $h$  correlated to the variation of  $\rho_1$ , in such a way that the quantity  $\Delta\rho gh$  is constant (conservation of salt) [Fig. 15(a)]. Huppert *et al.* [3] proposed the following expression for the position of the interface as a function of time:

$$h - \bar{z} = Bt^b = C_B \left[ \frac{\omega_g^3}{g'h} \right]^b t^b, \quad (14)$$

where  $\bar{z}$  is the mean position of the grid,  $\omega_g = 2\pi f_g$  is the frequency of the grid,  $g' = g(\rho_2 - \rho_1)/\rho_1$  is the reduced acceleration due to gravity, and  $b$  is an exponent lower than 1. They found  $b = 0.151 \pm 0.008$ , constant with  $\Delta\rho$  and  $f_g$  for a given stroke. Even though we found a higher discrepancy of the power  $b = 0.198 \pm 0.056$ , our values are in agreement with that found by Huppert *et al.* [3]. No clear dependency is observed either with respect to the initial value of  $\Delta\rho$

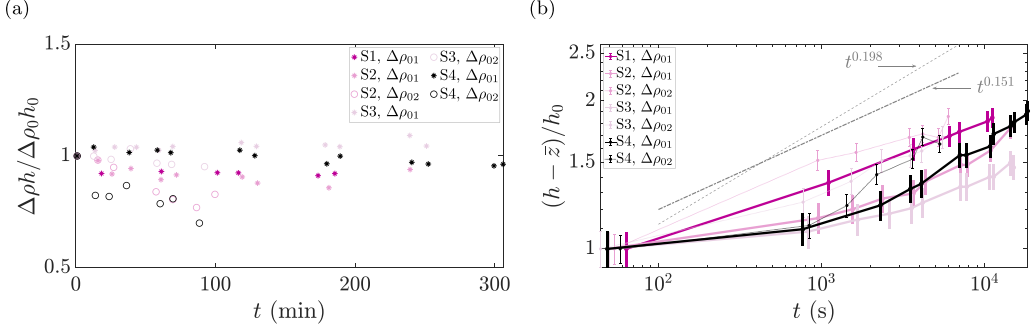


FIG. 15. (a) Time evolution of the density difference,  $\Delta\rho$ , multiplied by  $h$ . This quantity is normalized by its value at the initial time step,  $\Delta\rho_0 h_0$ . (b) Time evolution of the position of the interface,  $h$ , normalized by its initial value  $h_0$ . To compare with the power law proposed by Huppert *et al.* [3] (dash-dotted line), the mean position of the grid,  $\bar{z}$ , is subtracted from  $h$ .

or  $\text{Re}_g$  (not shown). The authors did not comment on  $C_B = B(g'h)^b / \omega_g^{3b}$ , which was a constant in their study. By dimensional analysis,  $C_B$  has to be proportional to a lengthscale at the power  $1 + 2b$ . Thus we tried to link  $C_B$  with characteristic lengthscales of our experiments, namely the stroke and the grid mesh. We tested four possible combinations, presented in Fig. 26 in Appendix F. The scaling depending only on the stroke leads to a relatively good prediction for  $C_b$  with a slight offset [Fig. 26(a)]. Combinations of both  $S$  and  $M$  are also possible for  $C_B$ , and the data seem closer to the slope 1 when adding the mesh size, as shown in Figs. 26(b)–26(d). The best agreement is found for the scaling  $SM^{2b}$ , for which all data collapse on the slope 1 [Fig. 26(d)]. Thus the temporal evolution of the position of the interface is best predicted by

$$h - \bar{z} = SM^{2b} \left[ \frac{\omega_g^3}{g'h} \right]^b t^b. \quad (15)$$

Regarding the time evolution of the interface thickness,  $\delta h$ , we verified that it reaches a steady state that is lower than its initial value (see Fig. 27 in Appendix F). The nearly steady value of  $\delta h$  is about  $0.1h$ , which is in agreement with Fernando and Long [25], and of the same order of the integral lengthscale of turbulence at the interface  $L_{\text{int}}^{\text{max}}$ . This indicates that the interface dynamics is controlled by the turbulence, but there could be some more complex equilibrium with molecular diffusion being stronger with a sharp density change [19].

### B. Entrainment law

As discussed in the Introduction, we seek to characterize the entrainment rate as a function of the Richardson number as in Eq. (7). Both quantities are based on turbulent flow properties that we consider in detail below. The Richardson number is usually defined as  $\text{Ri} = g\Delta\rho L_{\text{int}} / \rho_1 U_{\text{rms}}^2$ , with the rms velocity being the value in a homogeneous fluid, evaluated at the depth of the interface. Our results based on this convention are presented in Fig. 16(a). A power-law evolution of  $E$  with  $\text{Ri}$  seems to be a correct validation for each experiment, however there is no clear collapse of the different curves obtained for various values of the frequency and stroke for the grid in setup 1. For  $\text{Ri} < 1000$ , a power-law evolution with the power  $\gamma$  being between  $-1.2$  and  $-1.5$  seems to fit with our data. This tendency is in agreement with previous results [15,26]. For larger Richardson number ( $\text{Ri} > 1000$ ), another tendency is observed that tends to flatten. Despite a small number of points for  $\text{Ri} > 1000$ ,  $E$  seems to tend towards a constant value varying with the initial density difference [black dots in Fig. 16(a)]. It must be noted that past results that had a clear collapse of their data for mixing always corresponded to a constant stroke or frequency for the grid oscillation, which is not our case here.

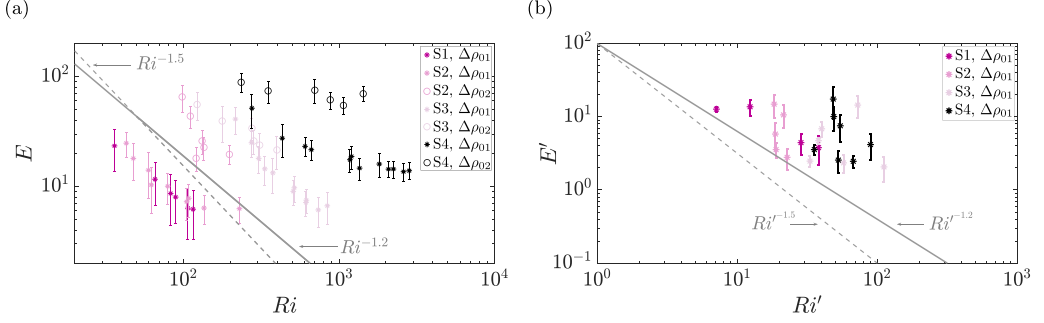


FIG. 16. (a) Entrainment rate,  $E$ , as function of the Richardson number,  $Ri$ . (b) Entrainment rate based on  $U_{\text{rms}}^{\text{max}}$  as function of the Richardson number,  $Ri'$ , based on the peak values of  $U_{\text{rms}}$  and  $L_{\text{int}}$  near the position of the interface.

We mentioned in the Introduction that  $U_{\text{rms}} \propto z^{-n}$ , with past studies discussing the appropriate value for  $n$  but always using this parametric law. Using this assumption, the definition of  $E$  in Eq. (7), and the expression in Eq. (14), Huppert *et al.* [3] demonstrated that the choice for  $n$  prescribes the exponent in the power law in the Richardson number, namely

$$\gamma = \frac{1 - b^{-1}}{2n} - \frac{1}{2}. \quad (16)$$

Based on power-law estimates for each case in Fig. 16(a), we can compare the values for  $\gamma$  from our experiments with respect to the theoretical prediction in Eq. (16), taking  $n = 1$  or  $5/2$ , this latter value having the best agreement with our observations for velocities in Sec. III B. On average, the evolution of the mixing rate for each experiment is better predicted when  $n = 5/2$ , although the comparison is not perfect (mismatch in the exponent of 20–60 %, not shown), which corresponds to  $\gamma = -1.51$  with  $b = 0.198$ . Although the exponent in the power law of Eq. (7) could be identified, the lack of collapse of the observations onto a single curve with variations of the experimental parameters (grid and fluid) leads us to consider alternative definitions for the relevant turbulent quantities to consider. Indeed, we have shown in Sec. IV C that the turbulence is altered at the interface, and it can modify the amplitude of the turbulent properties (especially  $U_{\text{rms}}$ ,  $k$ , and marginally  $L_{\text{int}}$ ) compared to the homogeneous fluid. Thus, we now evaluate the quantities in Eq. (7) based on the turbulent properties estimated at one integral scale from the interface ( $L_{\text{int}}^{\text{max}}$ ), where we observed a peak of intensity for  $L_{\text{int}}$  and  $U_{\text{rms}}$  in the two-layer case. Based on these two values, we define a new Richardson number and a new entrainment rate such as  $Ri' = g\Delta\rho L_{\text{int}}^{\text{max}} / \rho_1 U_{\text{rms}}^{\text{max}^2}$  and  $E' = U_e / U_{\text{rms}}^{\text{max}}$ . Our results are presented in Fig. 16(b). Note that there are fewer points than in Fig. 16(a) because we reported only data for which we did PIV measurements. Indeed, we are not able to predict  $U_{\text{rms}}^{\text{max}}$  from homogeneous fluid, as this parameter depends on both the stirring and the distance of the grid. On the one hand, using  $Ri'$ , data collapse better in a more continuous range of values, which is an indication that the use of a Richardson number based on local turbulent flow quantities ( $U_{\text{rms}}^{\text{max}}$  and  $L_{\text{int}}^{\text{max}}$ ) could be more appropriate to describe the mixing process. On the other hand, even though our data are in reasonable agreement with the power law  $-1.2$ , the scattering of the data is now greater, and uncertainties in the exponent are important.

### C. Remarks on the origin of mixing

Mixing in OGT is thought to be controlled by local and intermittent events associated with scales larger than the turbulence at the interface (supposedly based on internal wave properties) or by small coherent vortical structures [1]. Thanks to the large field of view and spatial resolution in our experiments, we were able to observe both the large-scale structures and the turbulent properties,

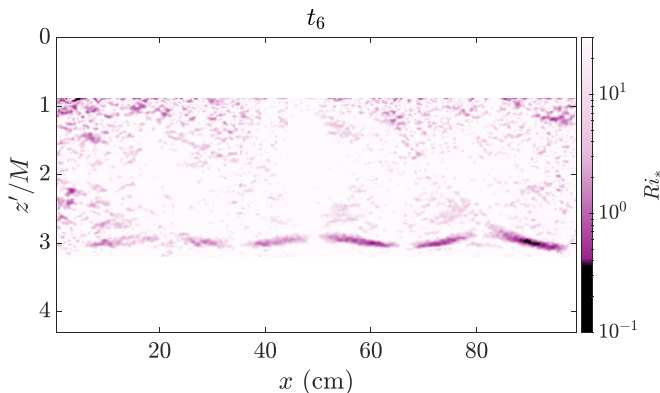


FIG. 17. Spatial map of the Richardson number,  $Ri_* = \frac{g'}{\delta h \nabla_z(\bar{u})}$ , based on the shear of the mean flow,  $\nabla_z(\bar{u})$ , interface thickness,  $\delta h$ , and the reduced gravity acceleration,  $g'$ , at  $t_6$  for S3 ( $\Delta\rho_1$ ).

and we discuss this aspect. The results obtained in the previous section suggest that the entrainment law can indeed be prescribed by a power law based on the relevant Richardson number, obtained by considering the true scales of the turbulent shear at the interface for a turbulent flow in a two-layer fluid ( $U_{\text{rms}}^{\text{max}}$  and  $L_{\text{int}}^{\text{max}}$ ).

Yet, as presented in Sec. IV A, we have also observed some mean flows in most of the cases studied, although the turbulent flow is the dominant feature in terms of kinetic energy ( $k \gg K$ ). These structures observed for the mean flow are very similar to downward jets. Mixing induced by a turbulent jet or plume incident on a two-layer fluid interface is a very similar topic of research, and it has been a challenging problem to identify the mechanisms at stake, as summarized in [40]. The entrainment law is then described based on the characteristic vertical velocity of the plume (or jet) at the interface,  $w_{\text{jet}}$ , and usually compared to a power law in Froude number  $Fr_i = w_{\text{jet}}/\sqrt{g' r_{\text{jet}}}$ , with  $r_{\text{jet}}$  the radius of the plume (or jet) at the interface, and  $g'$  the reduced gravity. Although our velocity measurements are in a plane that is not centered on the multiple jets observed, we can roughly estimate the value for the Froude number for each jet to be smaller than 1. This regime would thus be associated with intermittent internal wave breaking controlled by the mean shear generated by the jet. To confirm this scenario corresponding to the regime of mixing described in a recent study [41], we verify the stability of the interface deformation with respect to other mechanisms leading to mixing, Kelvin-Helmholtz (KH), or Holmboe (H) instabilities. We display the map of the Richardson number computed using the mean flow properties,  $Ri_* = \frac{g'}{\delta h \nabla_z(\bar{u})}$ , in Fig. 17, and we observe that the stability criteria for both of these instabilities are valid. Indeed, we do not see regions with values of  $Ri_*$  smaller than 1/4 (KH criterion) or larger than 30 (H criterion).

In the context of our study dedicated to OGT, it is impossible for us to discriminate mixing induced by shear-free turbulence only with shear-free turbulence in the presence of weak jetlike mean flows. More precisely, we cannot know if shear-free turbulence is altered by the jets leading to a different entrainment rate, or if entrainment due to shear-free OGT can be added independently to that due to turbulent plume. We consider that a better understanding of the amplification of  $U_{\text{rms}}$  at the interface could help greatly in answering this question.

## VI. CONCLUSIONS

In this paper, we have described the turbulent properties of shear-free turbulence induced by two different oscillating grid systems, i.e., in a homogeneous and a two-layer stratified fluid. In the case of OGT in a homogeneous fluid, our results are in good agreement with previous studies. We have improved the description of the turbulence decay with depth by considering a larger field of view,



and we have been able to verify that the description of Matsunaga *et al.* [10] is better suited to model the fast decay far from the grid, although it is not perfectly adjusted in terms of fitting parameters. Our measurements have provided a more complete description of all turbulent quantities based on a  $k$ - $\epsilon$  model, with a parametric form to prescribe them for a grid Reynolds number in the range [800, 12 500]. One noticeable improvement over previous studies is the description of the evolution with depth of the integral lengthscale  $L_{\text{int}}$  as a piecewise linear function of  $z$ , with a specific depth  $H_s$  at which a discontinuity occurs. Consequently, we found that the eddy viscosity  $\nu_t$  for OGT is better described as being almost constant over the depth range  $[0, H_s]$  before decreasing as a power law in  $z^{-3/2}$ . The use of  $\nu_t$  instead of  $k$  and  $\epsilon$  could be very useful to study other problems in OGT, such as mixing or the transport of a second phase in general (pollutants, particles), and we hope this characterization will be of interest for future studies.

We have also characterized OGT in the case of a two-layer fluid. We verify that the turbulent flow far from the interface ( $0 < z/h < 0.6$ ) is still comparable to OGT in a homogeneous fluid, although some variations of the fitting parameters with time can occur. Near the interface, differences with the case of a homogeneous fluid are observed. The loss of isotropy and the amplification of the turbulence near the interface are very similar to the observations made for a solid boundary [39] or in previous studies [23]. Peaks for the turbulent horizontal velocity, kinetic energy, and integral length are visible at a distance of  $L_{\text{int}}^{\text{max}}$  (max of the integral length with depth) or even less from the interface, before going to zero at the interface. Surprisingly, at the difference of the other turbulent quantities, the appropriate model for  $\nu_t$  in this fluid environment is a constant value with depth, until reaching the interface, where it goes to  $\nu_f$ . The value is reasonably well predicted by the homogeneous model we presented.

Finally, we investigate the mixing that also takes place when studying OGT in a two-layer fluid. The results on the evolution of the interface with time and the entrainment law as a function of the Richardson number are comparable with past studies, which systematically considered OGT in a homogeneous fluid as a reference for velocity and lengthscales [1,15,26]. Yet, the collapse of all observations on a simple law is not possible for various experimental cases with different strokes, frequencies, or density jumps. The entrainment law of the interface might be a function of the Richardson number only if the latter is associated with the turbulent flow properties measured at the interface and not from the properties deduced from homogeneous fluid cases. This “local” Richardson number near the interface is clearly controlled by the turbulence at the interface. It is also a challenging quantity to assess since it must be measured in the region of the fluid with the strongest density and velocity gradients. Furthermore, there are different mechanisms at stake in such experimental studies that can alter the values of this Richardson number. It could be due shear-free turbulence only, or it could be combined with other effects induced by weak mean flow resembling turbulent plumes. We suggest investigating this question in future studies focusing on mixing of a two-layer fluid with OGT combined with other controlled flow features (turbulent plumes, mean circulation, etc.).

## ACKNOWLEDGMENTS

The authors thank the technical support at Institut de Mécanique des Fluides de Toulouse (IMFT, UMR 5502) for visualizations (S. Cazin and M. Marchal) and experimental setup (J. D. Barron, H. Ayrolles, and F. Bergame). The authors also thank H. Michallet and M. Rastello for stimulating discussions.

## APPENDIX A: DEPTH PROFILES OF TURBULENT QUANTITIES IN HOMOGENEOUS FLUID FOR ANOTHER REYNOLDS NUMBER

In this Appendix, depth profiles of turbulent quantities obtained for a Reynolds number,  $Re_g$ , of 7980 are shown (Stirring H3 in Table I). More precisely, depth profiles of the turbulent kinetic energy  $k$  (Fig. 18), the integral lengthscale  $L_{\text{int}}$  (Fig. 19), the dissipation rate  $\epsilon$  (Fig. 20), and the

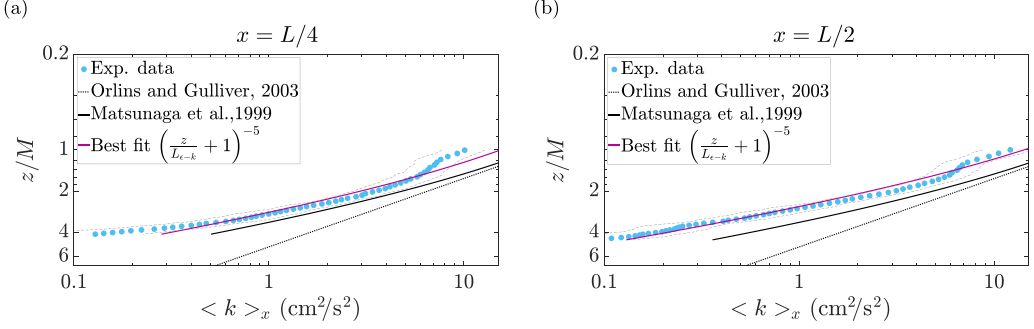


FIG. 18. Depth profiles of the turbulent kinetic energy,  $k$ , obtained in two laser sheets at (a)  $x = L/4$  and (b)  $x = L/2$  from the border of the tank. Symbols represent experimental data, with thin gray lines indicating the uncertainty in the values based on rms variations in  $k$ . Black lines represent models in Eqs. (2) and (3).

eddy viscosity  $\nu_t$  (Fig. 21) are shown. This experiment was performed in setup 2, being different from the one used for the case presented in the main part of the paper. It highlights that our approach does not depend on the geometry of the tank. Moreover, in this setup, images were recorded in two different laser sheets. They were located at  $x = L/4$  and  $L/2$  from the border of the tank, where  $L$  is the width of the tank. Thus, we also illustrate that our approach describes the OGT in the whole tank.

## APPENDIX B: DETAILS ON DISSIPATION RATE DEFINITIONS

The dissipation rate,  $\epsilon$ , which characterizes the turbulence decay is defined by the velocity gradients as

$$\epsilon = \nu_f \left( \frac{\partial u'_i}{\partial x_j} \frac{\partial u'_i}{\partial x_j} + \frac{\partial u'_i}{\partial x_j} \frac{\partial u'_j}{\partial x_i} \right). \quad (\text{B1})$$

From experimental data, access to the three components of the velocity is not always possible. Therefore, several methods exist to determine the dissipation rate. They are listed as follows:

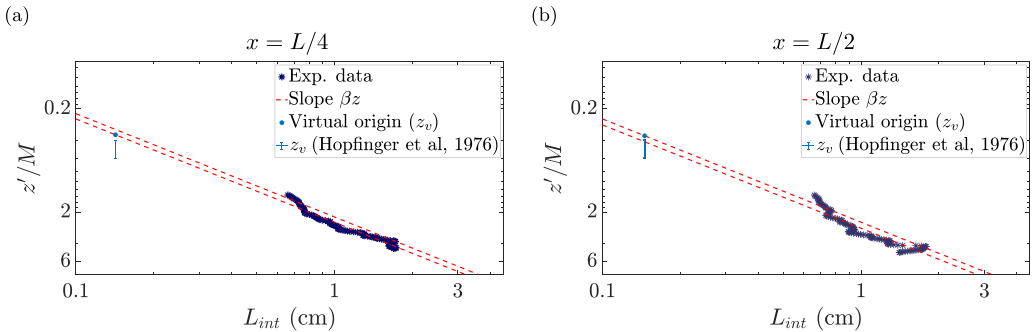


FIG. 19. Depth profiles of the integral lengthscale,  $L_{\text{int}}$ , obtained in two laser sheets at (a)  $x = L/4$  and (b)  $x = L/2$  from the border of the tank. The blue diamond is the virtual origin from the experimental data. The error bar is the virtual origin from [8]. Red dashed lines are Eq. (6) for two proportionality constants.

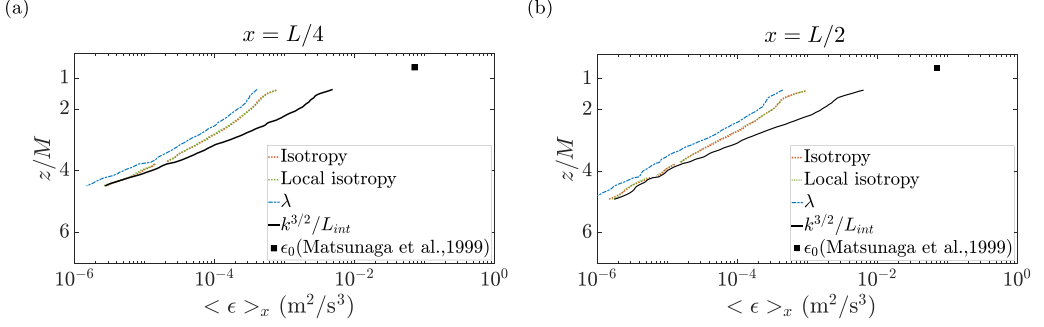


FIG. 20. Vertical profiles of the dissipation rate,  $\epsilon$ , calculated from four definitions with different assumptions. They were obtained in two laser sheets at (a)  $x = L/4$  and (b)  $x = L/2$  from the border of the tank.

(i) Assuming isotropy (i.e., the three velocity components are equal), the definition Eq. (B1) becomes

$$\epsilon = 15 \nu_f \left( \frac{\partial u'}{\partial x} \right)^2. \quad (\text{B2})$$

(ii) Assuming local isotropy (i.e., two velocity components are equal,  $u'$  and  $v'$  in our case) and using the continuity equation ( $\frac{\partial u'}{\partial x} + \frac{\partial v'}{\partial y} + \frac{\partial w'}{\partial z} = 0$ ), the definition Eq. (B1) becomes

$$\epsilon = 4 \nu_f \left[ \left( \frac{\partial u'}{\partial x} \right)^2 + \left( \frac{\partial w'}{\partial z} \right)^2 + \frac{\partial u'}{\partial x} \frac{\partial w'}{\partial z} + \frac{3}{4} \left( \frac{\partial u'}{\partial z} + \frac{\partial w'}{\partial x} \right)^2 \right]. \quad (\text{B3})$$

This assumption is usually made in the case of PIV 2D-2C measurements [30,36,37]. Note that Al-Homoud and Hondzo [30] and Doron *et al.* [36] found a factor of 3 in front of terms 1, 2, and 5 of the right-hand part of Eq. (B3). This was probably an error due to an omission of the factor 2 for the term  $\frac{\partial v'}{\partial y}$  in the definition of  $\epsilon$ . By doing the calculation again, we find the same expression as that found by De Jong *et al.* [37].

(iii) From the integral lengthscale,  $L_{\text{int}}$ ,  $\epsilon$  is expressed as follows [4,8,33,34]:

$$\epsilon = \frac{k^{3/2}}{L_{\text{int}}}. \quad (\text{B4})$$

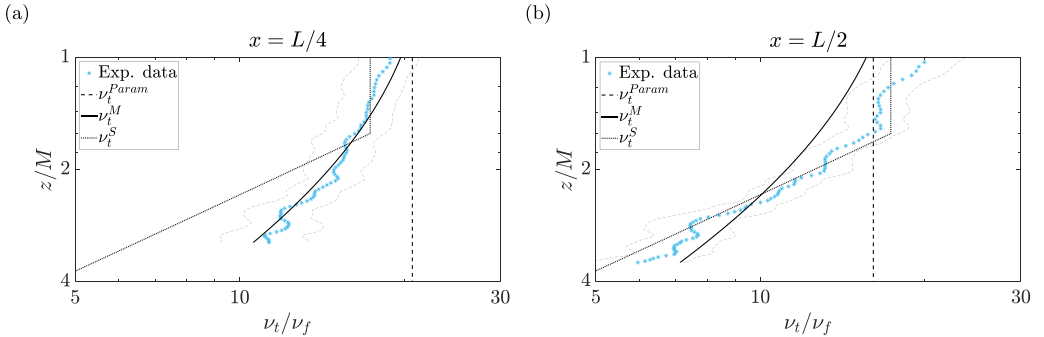


FIG. 21. Depth profiles of the eddy viscosity,  $\nu_t$ , obtained in two laser sheets at (a)  $x = L/4$  and (b)  $x = L/2$  from the border of the tank.  $\nu_t$  is normalized by the fluid kinematic viscosity  $\nu_f$ . Symbols are experimental data, with thin blue lines indicating the uncertainty in the values. Black lines are the parametric laws from Eqs. (9)–(11).

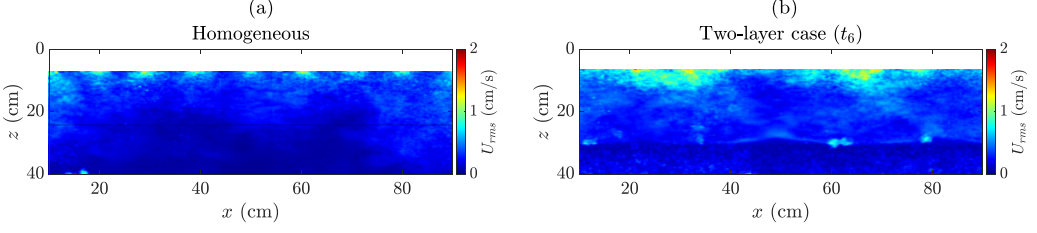


FIG. 22. Map of horizontal fluctuating velocity in (a) homogeneous fluid (case H12) and (b) two-layer fluid (case S3 at  $t_6$ ).

(iv) From the Taylor scale,  $L_T$ ,  $\epsilon$  is expressed as follows [34]:

$$\epsilon = 15\nu_f \frac{u'^2}{L_T^2}. \quad (\text{B5})$$

(v) From the power density spectrum (PDS) in the inertial domain,  $\epsilon$  is expressed as follows [10,38]:

$$\text{PDS} = C_\eta \epsilon^{2/3} k_x^{-5/3}. \quad (\text{B6})$$

Note that the inertial range should be covered over at least one or two decades to minimize the uncertainty on the slope and thus on  $\epsilon$ .

(vi) From the longitudinal structure function at order 2,  $D_{LL}(r)$  [33]. This corresponds to the covariance between the velocity difference between two positions in space  $x$  and  $x + dr$ . Based on the first and the second Kolmogorov similarity hypotheses, we can show that the structure function depends only on the dissipation rate such that [33,38]

$$\epsilon = \frac{1}{r} \left( \frac{D_{LL}(r)}{C} \right)^{3/2} \quad \text{with} \quad C = 2.12. \quad (\text{B7})$$

Note that in the case of homogeneous and/or isotropic flows, the authors use the instantaneous velocity field to compute  $D_{LL}$  and deduce  $\epsilon$ . Indeed, in these cases, the mean velocity is translation-invariant (or equal to zero in the case of isotropic flow). Therefore, as  $D_{LL}$  is deduced from a difference between two positions in space, using the instantaneous velocity field of the fluctuating field leads to the same expression. In our case,  $D_{LL}$  is directly calculated from the fluctuating velocity field.

### APPENDIX C: COMPARISON OF THE TURBULENT STRUCTURE NEAR THE GRID IN HOMOGENEOUS FLUID AND TWO-LAYER FLUID

Here we present maps of the horizontal fluctuation velocity, used to calculate the integral lengthscale. In a homogeneous fluid, the signature of the grid, with the presence of jets under each grid bar, is clearly visible [Fig. 22(a)], while in a two-layer fluid, two more prominent structures appear [Fig. 22(b)]. These differences in the flow could explain the different behavior observed for  $L_{\text{int}}$ , in particular its discontinuity at depth  $H_i$  in a homogeneous fluid. Note that in a homogeneous fluid, we observed the same signature of the grid for all cases. In two-layer fluid, the number of structures below the grid depends on the grid frequency, but they are always larger than the size of the grid bars. We could not explain the grid frequency dependence, but we verified that these structures are not grid eigenmodes.

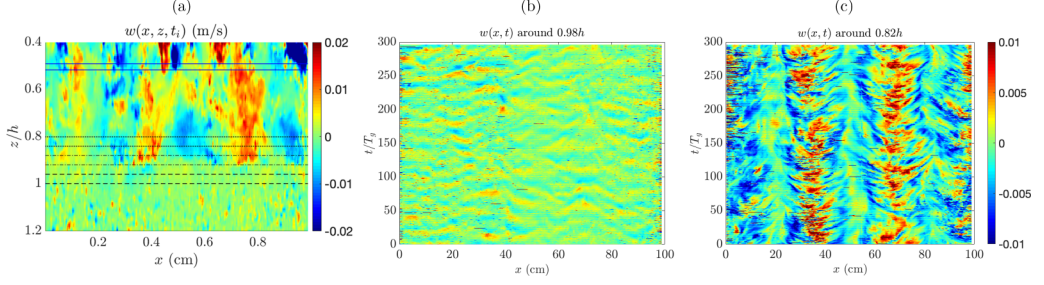


FIG. 23. Case S3,  $t_2$ . (a) Instantaneous vertical velocity field,  $w(x, z, t_i)$  around  $t_i/T_g \simeq 150$ , with indications on the domains for the extracted time series in (b) and (c), centered around  $z/h \simeq 0.98$  and  $z/h \simeq 0.82$ , respectively (between black lines, with a vertical extent of approximately  $0.04h$ ). The color bars for (b) and (c) are the same.

#### APPENDIX D: INTERNAL WAVES SIGNATURES IN TWO-LAYER FLUID FOR CASE S3

We discuss here some results on the internal wave dynamics near the interface for one specific case, S3 at time  $t_2$ . Similar results have been obtained at other times and for the other cases.

We first present in Fig. 23 the dataset investigated for internal wave dynamics. From instantaneous velocity measurements [panel (a)], we extract time series of horizontal and vertical velocities at some depth, with some averaging in the vertical velocity in between discontinuous black lines [panel (a)], to reduce the level of noise. Two resulting time series are shown in panels (b) and (c). An extra time series is extracted far away from the interface [ $z/h \simeq 0.5$  in between blue lines in panel (a)], which corresponds to a region described in the manuscript where the dynamics is similar to the case of a homogeneous fluid. Near the interface ( $z/h \simeq 0.98$ ), the amplitude of the flow features is of the order of  $2.5 \times 10^{-3}$  m/s, whereas farther away ( $z/h \simeq 0.82$ ), the amplitude of the more complex flow features corresponding to the superposition of waves, mean flow, and turbulent structures is four times larger.

From these time series at four depths above the interface, we compute the density spectrum with respect to the time of the velocity components at each horizontal location, and we average these quantities over the horizontal, denoted  $\langle E_{ww}^t \rangle_x$  and  $\langle E_{uu}^t \rangle_x$ . They are a function of  $f$  as shown in Fig. 24(a). Alternatively, we can also compute the density spectrum with respect to the horizontal coordinates at each frame, and we average these quantities over time, denoted  $\langle E_{ww}^x \rangle_t$  and  $\langle E_{uu}^x \rangle_t$ . They are function of  $k_x$  as shown in Fig. 24(b). Density spectra in two dimensions, which are

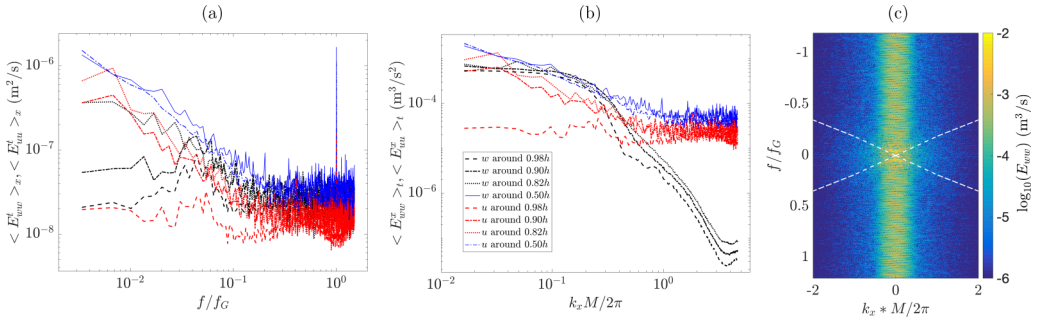


FIG. 24. Case S3,  $t_2$ . (a) Temporal and (b) spatial spectra of the time series extracted for  $u$  and  $w$  in the domains shown in Fig. 23, averaged over the (a) horizontal coordinate or (b) time. (c) Example of a two-dimensional spectrum for the vertical component of the velocity extracted  $z/h \simeq 0.9h$ . White dashed lines indicate the dispersion relation for internal waves in a two-layer fluid.

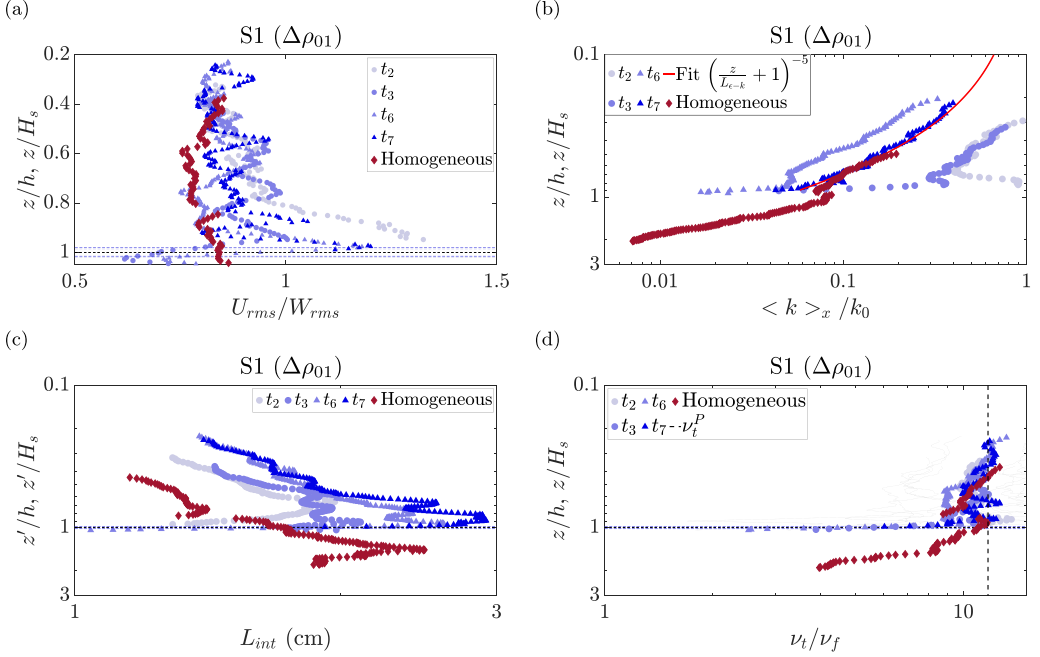


FIG. 25. Depth profiles of (a) the isotropy degree, (b) TKE, (c) integral lengthscale, and (d) turbulent eddy diffusivity, with the  $z$ -axis starting from the top position of the grid normalized by  $h$  for the two-layer fluid and by  $H_s$  for the homogeneous fluid; for case S1 ( $\Delta\rho_1$ ).

functions of  $f$  and  $k_x$  for the whole time series, could also be extracted but are quite noisy and tougher to interpret; an example is shown for the vertical velocity ( $E_{ww}$ ) at  $z/h \simeq 0.90$  in Fig. 24(c). One can notice that the signature of internal waves very near the interface (around  $z/h \simeq 0.9$ ) is the main contribution to the spectra of both horizontal and vertical velocities in the range  $[0.01, 0.06]f_G$  ( $[0.02, 0.12]$  Hz with  $f_G = 2$  Hz in the case shown, S3). Based on the dispersion relation of internal waves in a two-layer fluid, this corresponds to a wavelength of the order of 0.1–1 m, in good agreement with observations from Fig. 23. This is confirmed further by the fact that the associated energy is concentrated near the spectral domain for the dispersion relation of waves in an idealized two-layer fluid

$$\omega = \sqrt{\frac{\Delta\rho g}{\bar{\rho}} \frac{k_x}{\coth(k_x h_1) + \coth(k_x h_2)}} \quad (\text{D1})$$

[white dashed lines in Fig. 24(c)].

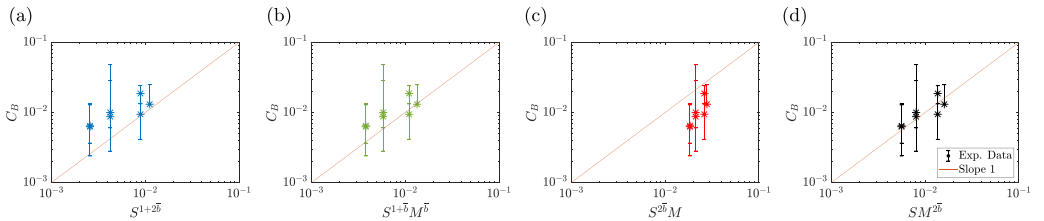


FIG. 26. Scaling laws of the parameter  $C_B$  as a function of the characteristic lengthscales of the device ( $S$  the stroke and  $M$  the grid mesh). Symbols are experimental data, and the red line is the slope 1. The mean value of  $\bar{b} = 0.198$  was taken.



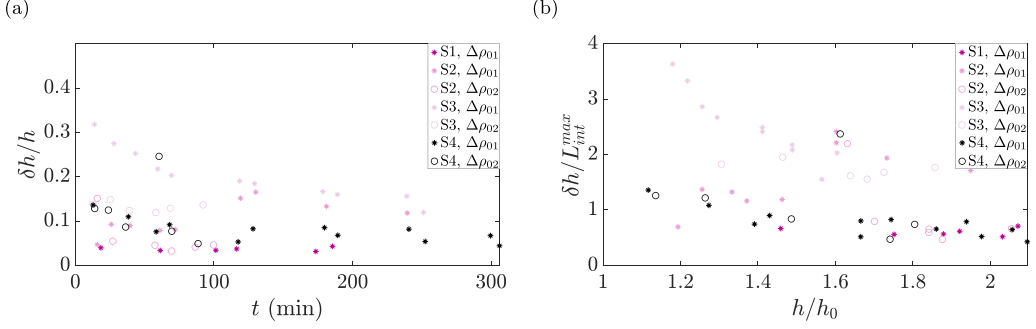


FIG. 27. (a) Time evolution of the interface thickness,  $\delta h$ , normalized by the interfacial position,  $h$ . (b) Evolution of  $\delta h$ , normalized by the maximum value of the integral lengthscale  $L_{int}^{max}$ , as a function of  $h$  normalized by the initial interfacial position,  $h_0$ .

Overall, the energy of the signal for internal waves is smaller than that due to turbulence above the interface ( $z/h \simeq 0.5$ ), or at most it is comparable when limiting the analysis to this specific frequency-wave-number spectral range.

#### APPENDIX E: DEPTH PROFILES OF TURBULENT QUANTITIES IN TWO-LAYER FLUID FOR CASE S1

Depth profiles of the turbulent quantities associated to case S1 of Table I, similarly to the results discussed in Sec. IV B, are shown Fig. 25.

#### APPENDIX F: MIXING—COMPLEMENTARY RESULTS

Related to the temporal evolution of the position of the interface, we try to estimate the dependency of  $C_B$  in Eq. (14) with the forcing parameters. We present four possible combinations in Fig. 26.

Regarding the temporal evolution of the interface thickness, we display it normalized by the position of the interface or the integral length in Figs. 27(a) and 27(b), respectively. Recall that  $\delta h$  is determined using conductivity measurements, being instantaneous density profiles. But due to local and intermittent distortions of the interface, regarding only instantaneous density profiles can lead to some aberrant points, as already noted in Ref. [26]. This can explain some scattering of the points in Fig. 27, even if the steady state should be reached (S4,  $\Delta\rho_2$ ).

- 
- [1] H. J. S. Fernando, Turbulent mixing in stratified fluids, *Annu. Rev. Fluid Mech.* **23**, 455 (1991).
  - [2] C. Wunsch and R. Ferrari, Vertical mixing, energy, and the general circulation of the oceans, *Annu. Rev. Fluid Mech.* **36**, 281 (2004).
  - [3] H. E. Huppert, J. S. Turner, and M. A. Hallworth, Sedimentation and entrainment in dense layers of suspended particles stirred by an oscillating grid, *J. Fluid Mech.* **289**, 263 (1995).
  - [4] H. Michallet and M. Mory, Modelling of sediment suspensions in oscillating grid turbulence, *Fluid Dyn. Res.* **35**, 87 (2004).
  - [5] J. Yan, N. S. Cheng, H. W. Tang, and S. K. Tan, Oscillating-grid turbulence and its applications: A review, *J. Hydraul. Res.* **45**, 26 (2007).
  - [6] S. J. Bennett, Y. Hou, and J. F. Atkinson, Turbulence suppression by suspended sediment within a geophysical flow, *Environ. Fluid Mech.* **14**, 771 (2014).

- [7] S. M. Thompson and J. S. Turner, Mixing across an interface due to turbulence generated by an oscillating grid, *J. Fluid Mech.* **67**, 349 (1975).
- [8] E. J. Hopfinger and J. A. Toly, Spatially decaying turbulence and its relation to mixing across density interfaces, *J. Fluid Mech.* **78**, 155 (1976).
- [9] I. P. de Silva and H. J. Fernando, Some aspects of mixing in a stratified turbulent patch, *J. Fluid Mech.* **240**, 601 (1992).
- [10] N. Matsunaga, Y. Sugihara, T. Komatsu, and A. Masuda, Quantitative properties of oscillating-grid turbulence in a homogeneous fluid, *Fluid Dyn. Res.* **25**, 147 (1999).
- [11] M. Rastello, H. Michallet, and J. L. Marié, Sediment erosion in zero-mean-shear turbulence, *Phys. Fluids* **32**, 036601 (2020).
- [12] M. Ura, T. Komatsu, and N. Matsunaga, Entrainment due to oscillating-grid turbulence in two-layered fluid, in *Turbulence Measurements and Flow Modeling*, edited by C. J. Chen, L.-D. Chen, and F. M. Holly, Jr. (Taylor and Francis, London, 1987), pp. 109–118.
- [13] N. S. Cheng and A. W. K. Law, Measurements of turbulence generated by oscillating grid, *J. Hydraul. Eng.* **127**, 201 (2001).
- [14] J. J. Orlins and J. S. Gulliver, Turbulence quantification and sediment resuspension in an oscillating grid chamber, *Exp. Fluids* **34**, 662 (2003).
- [15] R. I. Nokes, On the entrainment rate across a density interface, *J. Fluid Mech.* **188**, 185 (1988).
- [16] L. Verso, M. van Reeuwijk, and A. Liberzon, Steady state model and experiment for an oscillating grid turbulent two-layer stratified flow, *Phys. Rev. Fluids* **2**, 104605 (2017).
- [17] E. J. Hopfinger and P. F. Linden, Formation of thermoclines in zero-mean-shear turbulence subjected to a stabilizing buoyancy flux, *J. Fluid Mech.* **144**, 157 (1982).
- [18] H. Rouse and J. Dodu, Diffusion turbulente à travers une discontinuité de densité, *La Houille Blanche* **4**, 522 (1955).
- [19] P. F. Crapper and P. F. Linden, The structure of turbulent density interfaces, *J. Fluid Mech.* **65**, 45 (1974).
- [20] P. Linden, Mixing in stratified flows, *Geophys. Astrophys. Fluid Dyn.* **13**, 3 (1979).
- [21] Y. Zellouf, P. Dupont, and H. Peerhossaini, Heat and mass fluxes across density interfaces in a grid-generated turbulence, *Int. J. Heat Mass Transf.* **48**, 3722 (2005).
- [22] J. D. Woods and V. Strass, The response of the upper ocean to solar heating II: The wind-driven current, *Q. J. R. Meteorol. Soc.* **112**, 29 (1986).
- [23] I. A. Hannoun, H. J. Fernando, and E. J. List, Turbulence structure near a sharp density interface, *J. Fluid Mech.* **189**, 189 (1988).
- [24] J. S. Turner, The influence of molecular diffusivity on turbulent entrainment across a density interface, *J. Fluid Mech.* **33**, 639 (1968).
- [25] H. J. Fernando and R. R. Long, The growth of a grid-generated turbulent mixed layer in a two-fluid system, *J. Fluid Mech.* **133**, 377 (1983).
- [26] I. A. Hannoun and E. J. List, Turbulent mixing at shear-free density interface, *J. Fluid Mech.* **189**, 211 (1988).
- [27] M. Mory, A model of turbulent mixing across a density interface including the effect of rotation, *J. Fluid Mech.* **223**, 193 (1991).
- [28] H. J. S. Fernando and J. C. R. Hunt, Turbulence, waves and mixing at shear-free density interfaces. Part 1. A theoretical model, *J. Fluid Mech.* **347**, 197 (1997).
- [29] S. P. McKenna and W. R. McGillis, Observations of flow repeatability and secondary circulation in an oscillating grid-stirred tank, *Phys. Fluids* **16**, 3499 (2004).
- [30] A. Al-Homoud and M. Hondzo, Energy dissipation estimates in oscillating grid setup: LDV and PIV measurements, *Environ. Fluid Mech.* **7**, 143 (2007).
- [31] M. Rastello, H. Michallet, and J. L. Marié, Sediment erosion in zero-mean-shear turbulence, *Coastal Dyn.* **94**, 036601 (2017).
- [32] M. W. McCorquodale and R. J. Munro, A method for reducing mean flow in oscillating-grid turbulence, *Exp. Fluids* **59**, 182 (2018).
- [33] S. B. Pope, *Turbulent Flows*, Cambridge ed. (Cambridge University Press, Cambridge, 2000).

- [34] R. J. Adrian and J. Westerweel, *Particle Image Velocimetry*, 1st ed. (Cambridge University Press, Cambridge, 2011), p. 558.
- [35] S. J. Bennett, J. F. Atkinson, Y. Hou, and M. J. Fay, Turbulence modulation by suspended sediment in a zero mean-shear geophysical flow, [Coherent Flow Struct. Earth's Surf.](#) **20**, 309 (2013).
- [36] P. Doron, L. Bertuccioli, J. Katz, and T. R. Osborn, Turbulence characteristics and dissipation estimates in the coastal ocean bottom boundary layer from PIV data, [J. Phys. Oceanogr.](#) **31**, 2108 (2001).
- [37] J. De Jong, L. Cao, S. H. Woodward, J. P. Salazar, L. R. Collins, and H. Meng, Dissipation rate estimation from PIV in zero-mean isotropic turbulence, [Exp. Fluids](#) **46**, 499 (2009).
- [38] D. Xu and J. Chen, Accurate estimate of turbulent dissipation rate using PIV data, [Exp. Therm. Fluid Sci.](#) **44**, 662 (2013).
- [39] M. W. McCorquodale and R. J. Munro, Experimental study of oscillating-grid turbulence interacting with a solid boundary, [J. Fluid Mech.](#) **813**, 768 (2017).
- [40] A. B. Shrinivas and G. R. Hunt, Confined turbulent entrainment across density interfaces, [J. Fluid Mech.](#) **779**, 116 (2015).
- [41] J. Herault, G. Facchini, and M. Le Bars, Erosion of a sharp density interface by a turbulent jet at moderate froude and reynolds numbers, [J. Fluid Mech.](#) **838**, 631 (2018).